JOURNAL OF GEOPHYSICAL RESEARCH, VOL. 105, NO. C11, PAGES 26,203–26,224, NOVEMBER 15, 2000

The generation of internal waves on the continental shelf by Hurricane Andrew

Timothy R. Keen

Naval Research Laboratory, Oceanography Division, Stennis Space Center, Mississippi

Susan E. Allen

Department of Earth and Ocean Sciences, University of British Columbia, Vancouver, Canada

ABSTRACT. Observed currents, temperature, and salinity from moored instruments on the Louisiana continental slope and shelf reveal multiple baroclinic oscillations during Hurricane Andrew in August 1992. These measurements are supplemented by numerical models in order to identify possible internal wave generation mechanisms. The Princeton Ocean Model is run with realistic topography, stratification, and wind forcing to extend the observations to Mississippi Canyon and other areas on the shelf. A two-layer isopycnal model is used with idealized topography and spatially uniform winds to isolate internal waves generated in and around the canyon. The combination of the observations and the results from the numerical models indicates several possible mechanisms for generating long internal waves: (1) near-inertial internal waves were generated across the slope and shelf by dislocation of the thermocline by the wind stress; (2) interaction of inertial flow with topography generated internal waves along the shelf break, which bifurcated into landward and seaward propagating phases; (3) downwelling along the coast depressed the thermocline; after downwelling relaxes, an internal wave front propagates as a Kelvin wave; and (4) Poincaré waves generated within Mississippi Canyon propagate seaward while being advected westward over the continental slope. These processes interact to produce a three-dimensional internal wave field, which was only partly captured by the observations.

1. Introduction

The dominant continental shelf response to a tropical cyclone is barotropic, including the generation of a Kelvin-like coastal storm surge and continental shelf waves [*Fandry et al.*, 1984; *Hearn and Holloway*, 1990; *Fandry and Steedman*, 1994]. Kelvin waves are restricted to the transient wave front [*Grimshaw*, 1988; *Tang and Grimshaw*, 1995]. The variable wind stresses during hurricanes also generate subinertial shelf waves (frequency $\omega < |f|$, where f is the local inertial frequency), which dominate the large-scale barotropic response [*Huthnance*, 1978; *Tang et al.*, 1997]. In examining observations of storm flows, however, the influence of baroclinic processes on continental shelf oceanography is also apparent [e.g., *Hazelworth*, 1968; *Smith*, 1982]. The most complete documentation of these effects is available for Hurricane Andrew [*Cardone et al.*, 1994] (hereinafter referred to as C94).

Hurricane Andrew made landfall southwest of New Orleans, Louisiana, at approximately 0900 UT on August 26, 1992 (Figure 1). While transiting the continental shelf, the hurricane eye crossed over moored instrument arrays maintained by the Louisiana-Texas (LATEX) oceanography program, National Oceanic and Atmospheric Administration (NOAA) meteorological buoys and Coastal-Marine Automated Network stations, and commercial oil platforms. The resulting observations of winds, waves, currents, temperature, salinity, and coastal water depth during the hurricane have been discussed by C94.

The oceanographic response to Hurricane Andrew was both barotropic and baroclinic. *Keen and Glenn* [1999] (hereinafter referred to as KG99) discuss shallow water currents during the directly forced stage of the storm and demonstrate the importance of baroclinic flow. They focus on four processes directly related to the generation of baroclinic oscillations: (1) turbulent mixing, (2) trapped coastal waves, (3) near-inertial oscillations, and (4) upwelling and downwelling coastal flows. Turbulent mixing was strong within 1 R_w (radius of maximum winds) of the hurricane eye. This distance was about 40 km immediately prior to landfall. Consequently, stratification was eliminated near the coast, whereas the pycnocline was undisturbed at distances greater than 2 R_w. The resulting internal wave field was highly variable within the storm region.

Large-scale meteorological forcing such as extratropical cyclones can be treated as linear fronts [see *Kundu*, 1986]. The coastal response to such an impulsive wind consists of a locally forced oscillation within the upper layer and long barotropic and baroclinic gravity waves generated at the coast, which dominate in the lower layer [*Millot and Crepon*, 1981]. Consequently, the near-surface inertial wave field may be two dimensional in plan view [*Smith*, 1989]. The wind fields associated with tropical cyclones cannot be treated as lines, however, because of their small spatial scale. Thus the internal wave field will be three dimensional even near the surface.

This paper examines the generation of internal waves on the Louisiana continental shelf and slope during Hurricane Andrew

Paper number 2000JC900137.
0148-0227/00/2000JC900137$09.00

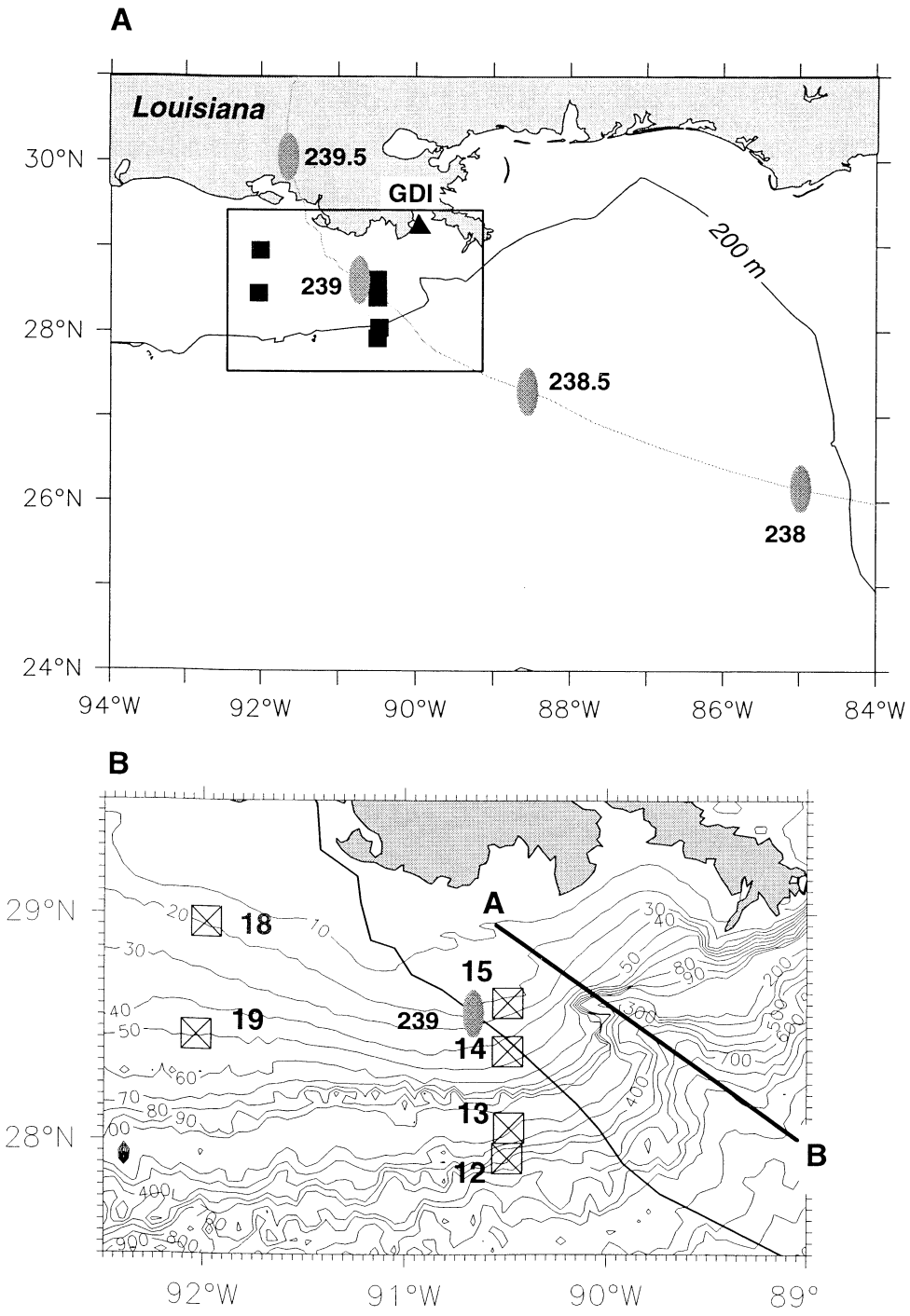

Figure 1. (a) Map showing track of Hurricane Andrew and location of the eye (labels are Julian day). GDI is Grand Isle. (b) Inset map showing LATEX moorings and cross-section A-B referred to in text and Plates 2 and 3. The cross section goes down the axis of Mississippi Canyon.

using both observations and numerical models. The observational evidence from the LATEX moorings is presented in section 2. However, because of the limited area coverage of the data and the complexity of the coastal response, a baroclinic, primitive equation numerical model with realistic topography, stratification, and wind forcing is used to examine internal wave generation in section 3. A comparison of the model with the observations shows that it reproduces internal waves within the frequency band of interest sufficiently to be a useful tool to examine generation mechanisms where observations are unavailable. This model is then used to examine possible internal wave generation within Mississippi Canyon, which is located near the storm track. The results from the realistic numerical model are complex, however, making it difficult to evaluate smaller-amplitude internal waves. Thus in section 4 we

present results from an idealized numerical model. This model isolates the influence of alongshore variations in topography and the time dependence of the wind field. The implications from the observations, the realistic numerical model, and the idealized model are discussed in section 5.

2. Baroclinic Oscillations Observed on the Shelf and Slope

The LATEX moorings (see Table 1 for depths and Figure 1 for locations) are located along two lines on the Louisiana continental shelf and slope. The eastern array consists of four moorings in water depths from 505 m to 20 m. A second array located 150 km to the west has moorings in water depths of 51 m and 18 m. The temperature and salinity profiles at mooring 12 (Figure 2) on August 24 (Julian day (JD) 237) are representative of stratification before the storm (C94). There was a thermocline at 20 m, but the mixed layer depth indicated by the salinity profile was only 10 m. The buoyancy frequency N is greatest at the thermocline, where high-frequency internal waves ($N = 25$ cycles per hour (cph)) would be generated. However, the sampling interval of 30 min does not resolve any of these internal waves.

The inertial period (IP) at the latitude of the moorings ranges from 25.9 hours (frequency of 0.927 cycle per day (cpd)) to 26.4 hours (frequency of 0.909 cpd). In this paper, we refer to frequencies within 20% above the local inertial frequency f as near inertial (see *Kundu* [1976] for a discussion). The inertial period is very similar to the diurnal O_1 astronomical tidal period of 25.8 hours (frequency of 0.93 cpd). Because of the similarity in the inertial and O_1 tidal frequency, all observed time series of currents had the five largest tidal components (M_2, S_2, N_2, K_1, and O_1) removed (C94).

Inertial flows are correlated with synoptic wind forcing on the Louisiana shelf [*Chen et al.*, 1996; *Chen and Xie*, 1997]. Forced near-inertial oscillations are generated when variations in the wind stress are in phase with near-inertial oscillations in the mixed layer [*Schott*, 1971]. When this occurs, the oscillations will reach maximum amplitude. During Hurricane Andrew, the wind vectors rotated counterclockwise (CCW) on the western side of the storm track, and thus no correlation is expected. The wind rotated clockwise (CW) at near the inertial frequency along the storm track. The CW rotation increased away from the track to the east and was twice the inertial frequency at Grand Isle (see Figure 1 for location). Consequently, the wind rotation and the near-inertial oscillations are not directly correlated at moorings located more than 1 R_w east of the storm track. We thus expect to find the maximum near-inertial oscillation amplitudes in the observations from near the storm track.

This section presents evidence for baroclinic oscillations using time series of currents, temperature, and salinity at the moorings listed in Table 1. The frequency dependence of these data is examined by using power spectra of the observations. Previous observational and modeling studies show that the following waves should be present: (1) barotropic edge waves and continental shelf waves [*Fandry and Steedman,* 1994], (2) barotropic and baroclinic Kelvin waves [*Fandry et al.,* 1984; *Beletsky et al.,* 1997], (3) inertial waves [*Chen et al.,* 1996], and (4) superinertial internal waves [e.g., *Niwa and Hibiya,* 1997]. It is not expected that all of these oscillations will be discernible from the observations, however, because of the presence of dominant waves and a background spectrum. It therefore will be necessary to use numerical models to further elucidate the generation of baroclinic oscillations during the storm.

2.1. Current Vectors

The time series of currents measured at the LATEX moorings are presented in Figure 3. The power spectra of current magnitudes (Figure 4) were calculated by using fast Fourier transforms (FFT) after removing the mean. The sampling interval is 30 min. These data will be used to analyze baroclinic oscillations generated by the hurricane's passage. The lower frequencies (less than 0.35 cpd) are expected to be aliased because of the record length of only 10 days. This very low frequency motion will not be discussed.

The current magnitudes at both meters at mooring 12 (Figure 3a) reveal a strong oscillation at near the inertial frequency (Figure 4a). The current vectors rotated CW, with the surface and bottom currents 180° out of phase (Figure 3b). Plotting these currents by using hodographs (not shown) indicates a mean southwesterly barotropic current parallel to isobaths, with surface currents greater than 0.3 m s^{-1} after the storm peak. The power peak at 0.375 cpd indicates subinertial barotropic motion with a period of 64 hours. The current variance decreases steadily at superinertial frequencies. For most of the moorings, this high-frequency motion is significantly less than the near-inertial and subinertial bands. Although these internal waves are important, it is not practical to closely examine them in the present study. Thus we limit our discussion to internal waves with near-inertial and subinertial periods only.

Table 1. Location of Louisiana-Texas Current Meters for This Study

Mooring	Longitude, °W	Latitude, °N	Meter Depth, m	Water Depth, m
12	90.494598	27.923870	12, 100	505
13	90.485878	28.057529	12, 100, 190	200
14	90.492867	28.394569	11, 37,	47
15	90.491577	28.608299	10, 17,	20
18	91.982719	28.962730	10, 19,	22
19	92.034798	28.465170	3, 47,	51

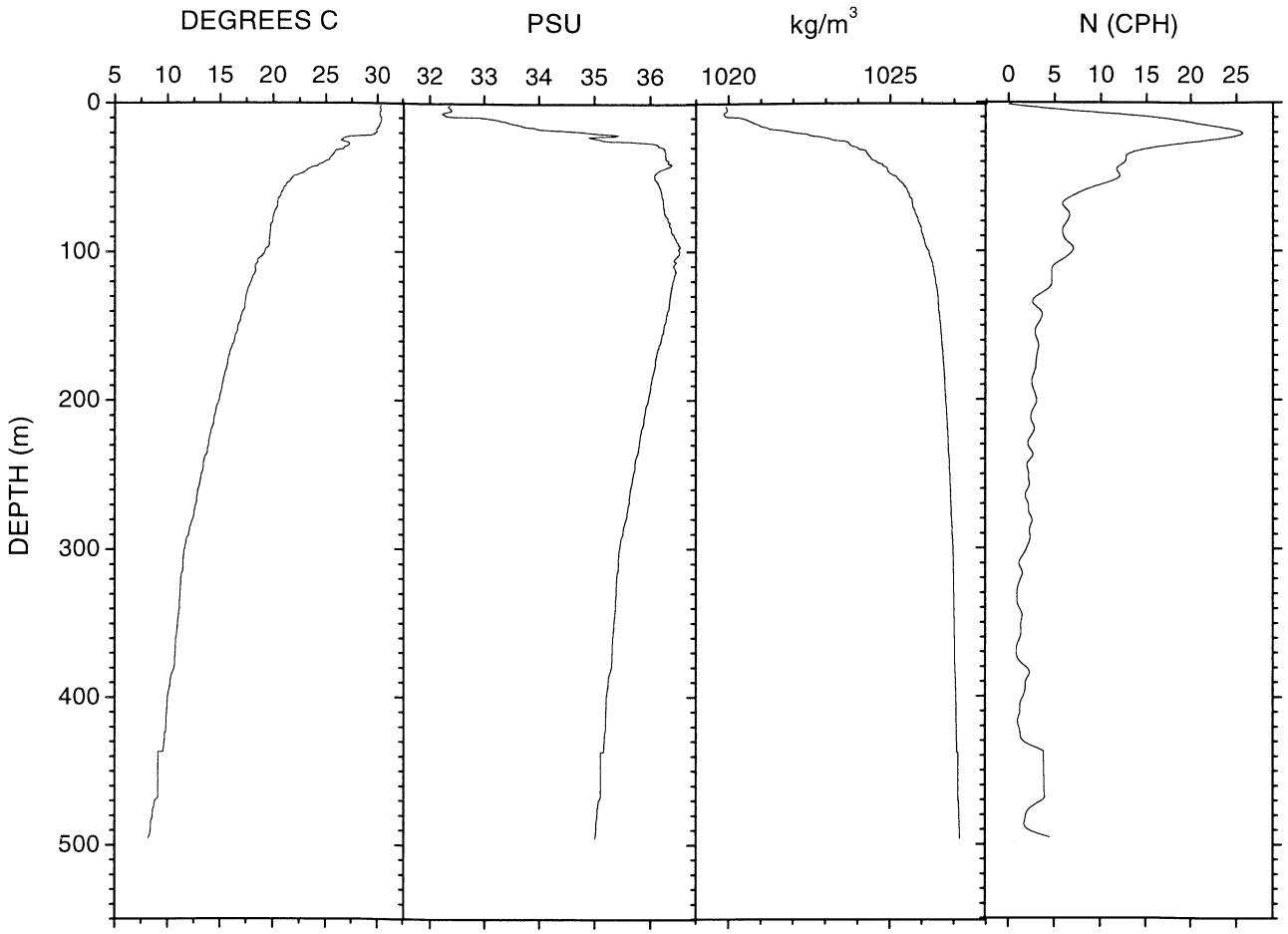

Figure 2. Profiles of temperature, salinity, density, and buoyancy frequency at mooring 12 on JD 237 (August 24).

Using 8 months of observations at the LATEX moorings, *Chen et al.* [1996] found that near-inertial oscillations are greatest at mooring 13 and decrease both landward and seaward. This appears to be the case for the hurricane flow as well. The strongest and most recognizable near-inertial oscillations were generated at mooring 13. The surface currents reached 1.25 m s^{-1} after 1 IP, at which time bottom currents exceeded 1 m s^{-1}. After 2 IPs, the surface and bottom current amplitudes were in phase for the duration of the measurements. Like the currents at mooring 12, a CW inertial rotation continued throughout the observation period (Figure 3b). The power spectrum (Figure 4b) indicates that the largest variance is associated with a strong near-inertial peak at 0.93 cpd, corresponding to a period of 25.8 hours. Note the superposition of this motion on the O_1 tide. The current variance in the subinertial band is broadly distributed and significantly less than that in the near inertial.

The surface currents at mooring 14 contain oscillations that are initially in phase with mooring 13. The surface current variance (Figure 4c) is greatest at the near-inertial frequency of 1.03 cpd (period of 23.3 hours). The inertial currents below the mixed layer have an initial phase lag of 6 hours, but they are damped within a few days. The subinertial peak at 0.468 cpd (period of 51 hours) is the dominant frequency at the lower current meter instead. This peak appears to represent a barotropic flow. Moorings 13 and 14 are 37.5 km apart, which is very close to R_w for the hurricane. The correlation between the initial response at moorings 13 and 14 thus implies that the storm wind field simultaneously generated the initial mixed layer perturbation at these moorings on August 26.

The upper current meter failed at mooring 15 (Figure 3a) and the record is incomplete. The currents appear to be barotropic prior to failure, however. The dominant power peak (Figure 4d) at 0.468 cpd is also present at mooring 14.

The along-shelf correlation distance for the LATEX shelf is about 300 km [*Chen et al.*, 1996], but the length scale for the storm, R_w, is only 40 km (KG99). Thus the correlation between currents at the eastern and western moorings is expected to be insubstantial. Mooring 18 is located approximately 2 R_w west of the storm track, and consequently, the storm currents (Figure 3a) were weaker. Surface flow was to the west (Figure 3b) for most of the measurement interval except on JD 239, when the strongest currents were eastward in response to the local wind stress. The current variance (Figure 4e) at the surface is distributed between near-inertial and subinertial frequencies.

The dominant power peak (Figure 4f) for surface currents at mooring 19 is at 0.75 cpd (period of 32 hours). Inertial motion is weaker than subinertial, but CW rotation is apparent in the current direction at the bottom after JD 236 (Figure 3b), becoming important at the surface after JD 240. The current variance at the bottom is also greatest at 0.75 cpd, as at mooring 13, but the inertial peak is smaller. Subinertial motion at both meters also occurs at 0.468 cpd, which is dominant at the lower current meter. This low-frequency motion is present at both western moorings, as well as

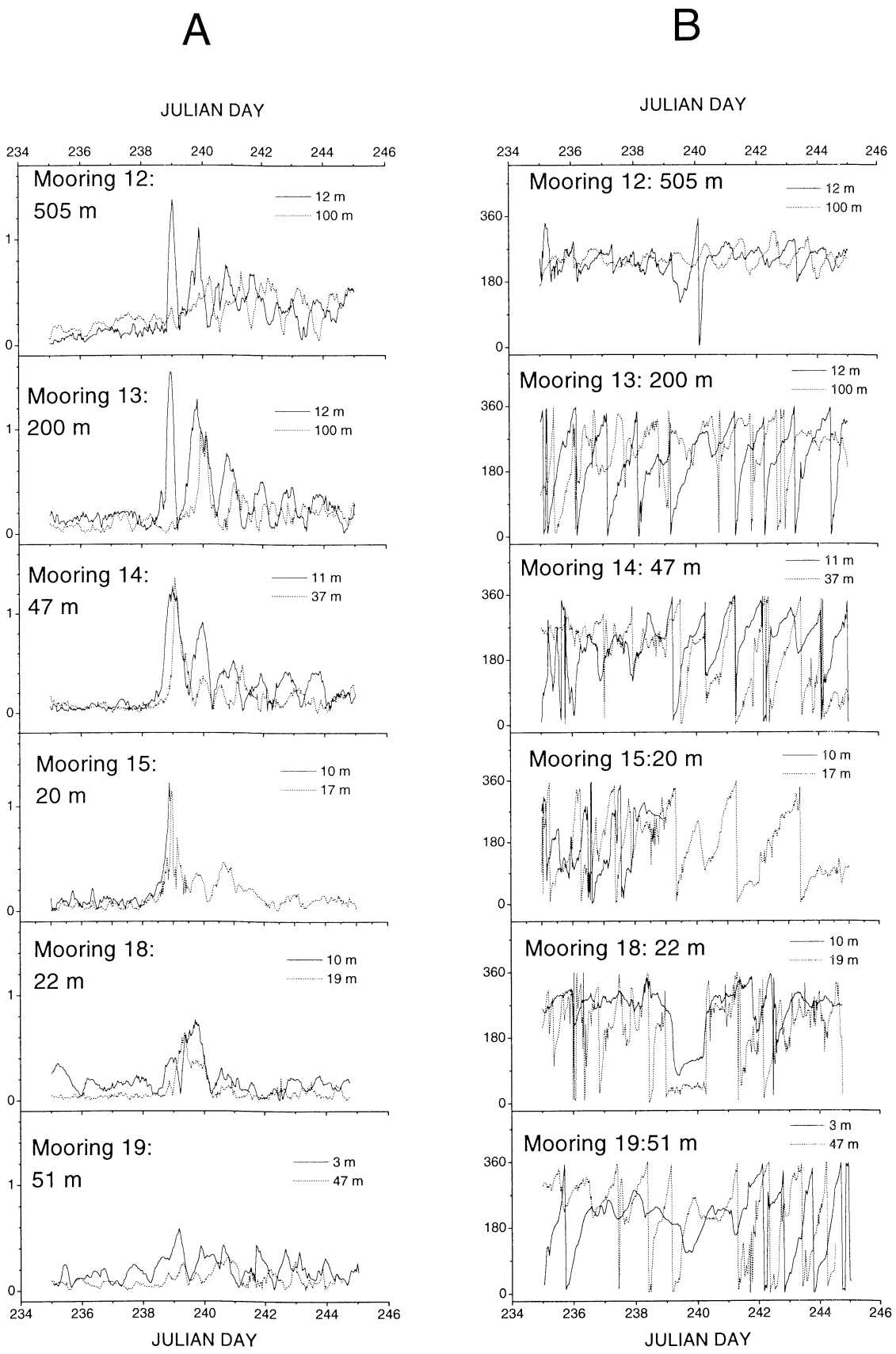

Figure 3. Time series of observations at the LATEX moorings. (a) Current magnitudes in meters per second. (b) Current direction, in degrees clockwise from north.

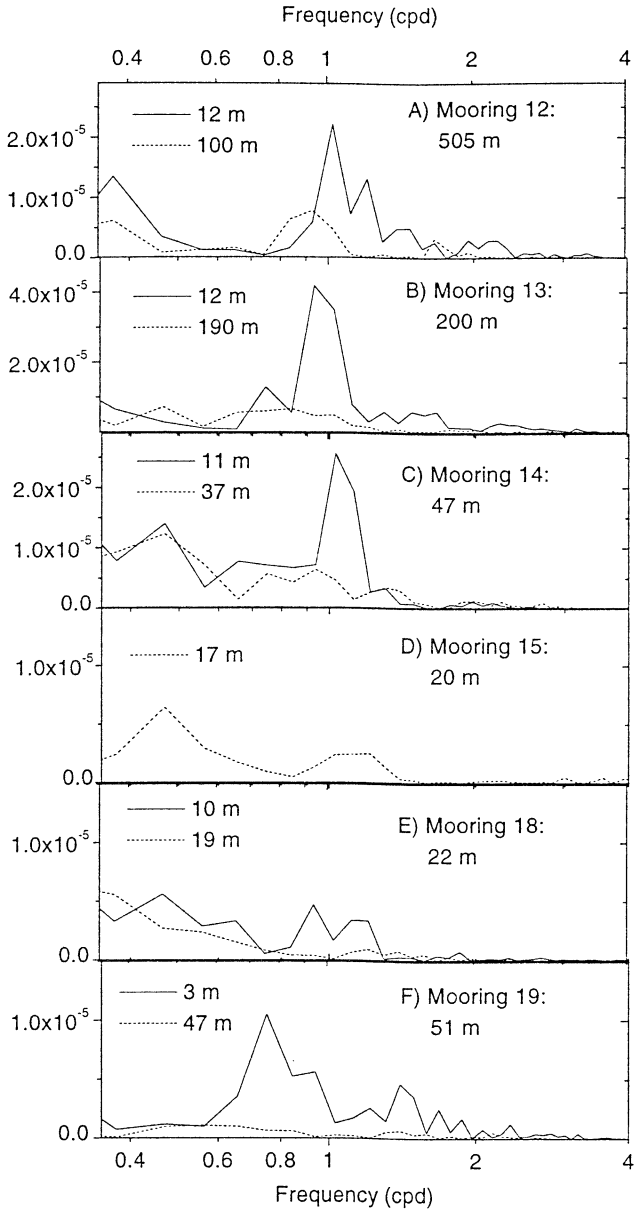

Figure 4. Power spectra for observed currents at LATEX moorings. Units are $m^2 s^{-2}$. See Figure 1 for locations.

moorings 14 and 15. It may be associated with a barotropic shelf wave as described by *Hearn and Holloway* [1990].

2.2. Temperature

The astronomical tidal signal cannot be easily removed from temperature and salinity time series because of nontidal variability. There is, therefore, no way of unambiguously differentiating near-inertial frequency variability at around 0.93 cpd from the O_1 tidal signal in most cases. This is partly caused by the choice of frequency bins used in the FFT method. Thus this discussion will not closely examine frequencies of either 0.93 cpd or 0.9375 cpd. Higher and lower frequencies are considered safely distanced from the O_1 signal, however.

The near-surface temperature at mooring 12 (Figure 5a) was increasing as the storm approached on JD 238 (August 25). A rapid decrease of 4°C on JD 239 followed the maximum surface current (Figure 3a) by 8 hours. A second pulse occurred 26.5 hours later. There is no power peak (Figure 6a) at a frequency of 0.905 cpd, however. Instead, the largest peak is located at 0.6525 cpd (period of 36.78 hours).

The upper meter at mooring 13 (Figure 5b) recorded a steady drop of 6°C between JD 237 and JD 242, and there is no distinct near-inertial peak (Figure 6b). Instead, internal wave energy is distributed across the spectrum. The initial temperature response at 100 m was also weak, but near-inertial oscillations developed on JD 239. A near-inertial peak at 1.03 cpd dominates the temperature power spectrum below the mixed layer.

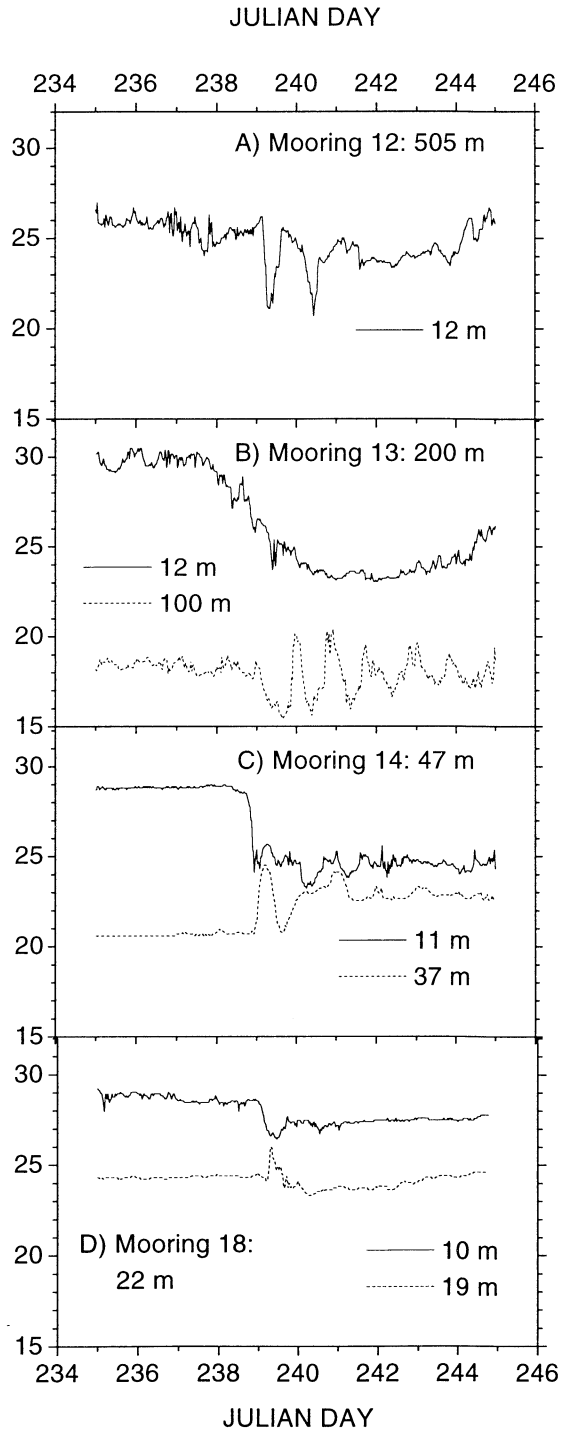

Figure 5. Temperature time series of observations at LATEX moorings. Units are degrees Celsius.

Turbulent mixing reduced the surface temperature at mooring 14 by 5°C (solid line in Figure 5c) on JD 238. This mixing was not immediately seen at the lower meter (dashed line), however, where the temperature did not begin to increase until the surface temperature reached a minimum of 24°C. The temperature at the lower meter subsequently increased rapidly by 4°C on JD 239 just as a 1°C spike was observed near the surface. The occurrence of this peak at both meters indicates strong downward deflection of isotherms, but the source of this disturbance cannot be identified from these data alone. It may represent an internal wave as hypothesized by *Keen and Glenn* [1999] or a response to the local wind stress. There was a net increase of 2°C at the lower meter on JD 239, which is very likely caused by local turbulent mixing. The dominant peak for the lower gauge (dashed line in Figure 6c) is at 1.125 cpd, which is 18% above the local inertial frequency. It is therefore within the near-inertial band [*Kundu*, 1976]. The lack of a spectral peak at this frequency for the upper meter suggests that the initial temperature response at mooring 14 was only weakly inertial.

The upper meter at mooring 18 (Figure 5d) reveals turbulent mixing and overshoot, with subsequent relaxation to local conditions. The time series at the lower meter (dashed line in Figure

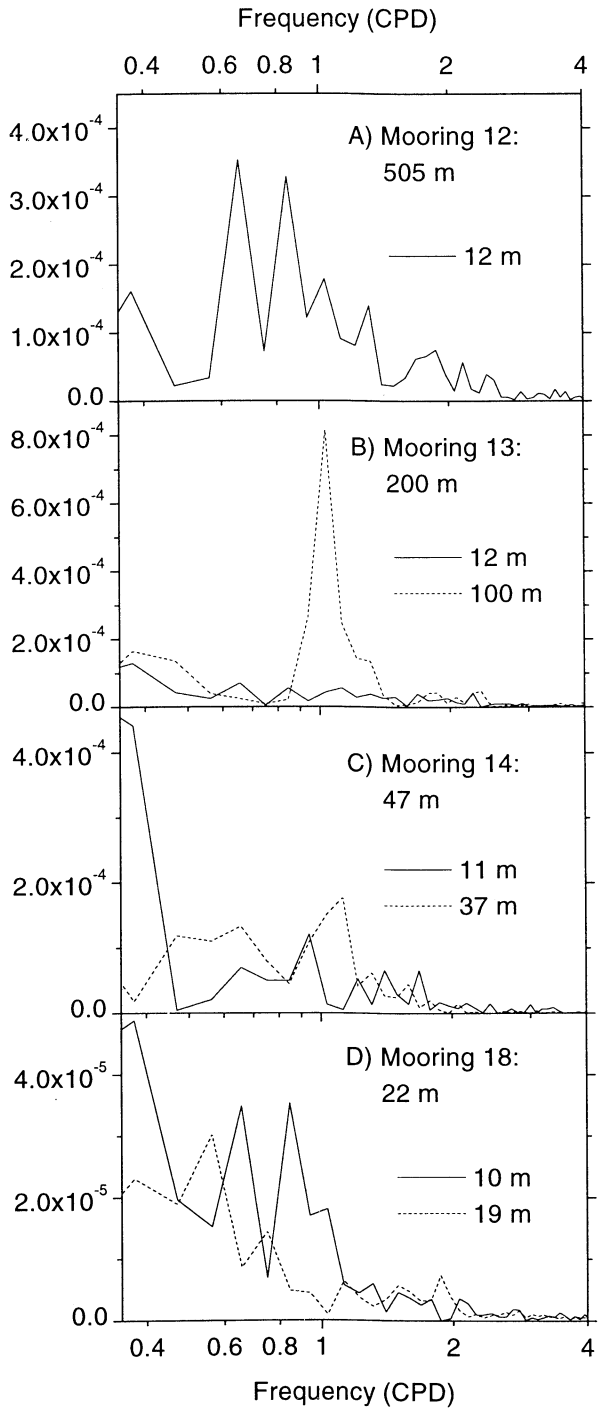

Figure 6. Power spectra of observed temperature time series from the LATEX moorings. Units are $(°C)^2$.

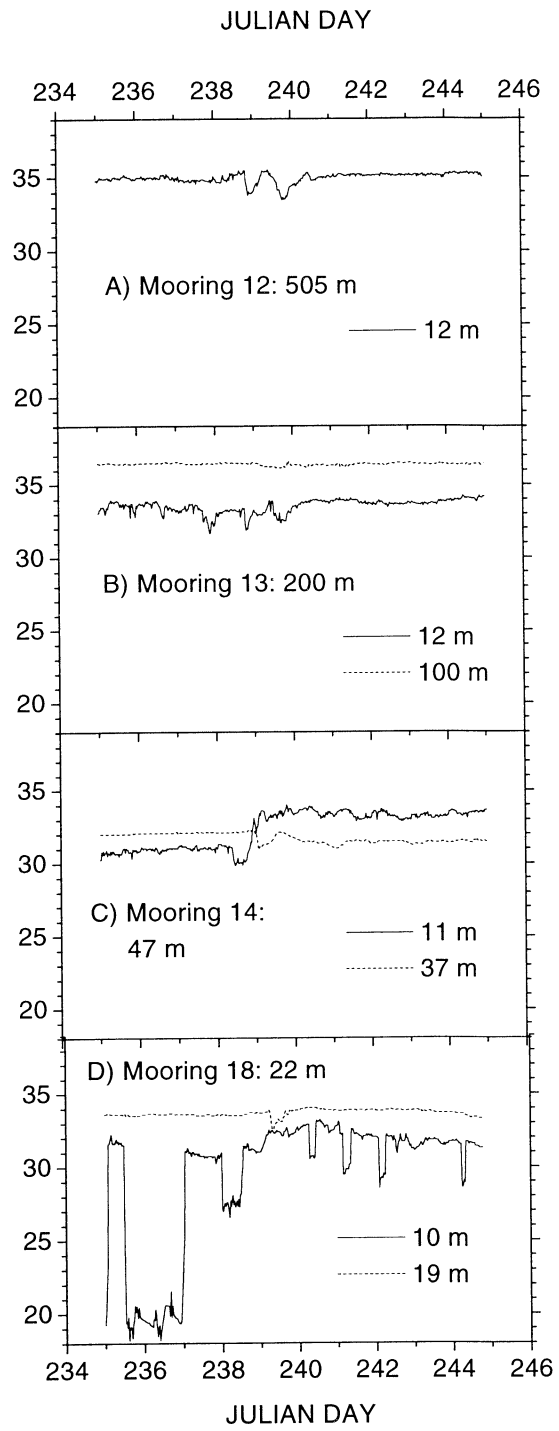

Figure 7. Salinity time series observed at LATEX moorings. See Figure 1 for locations. Units are practical salinity units.

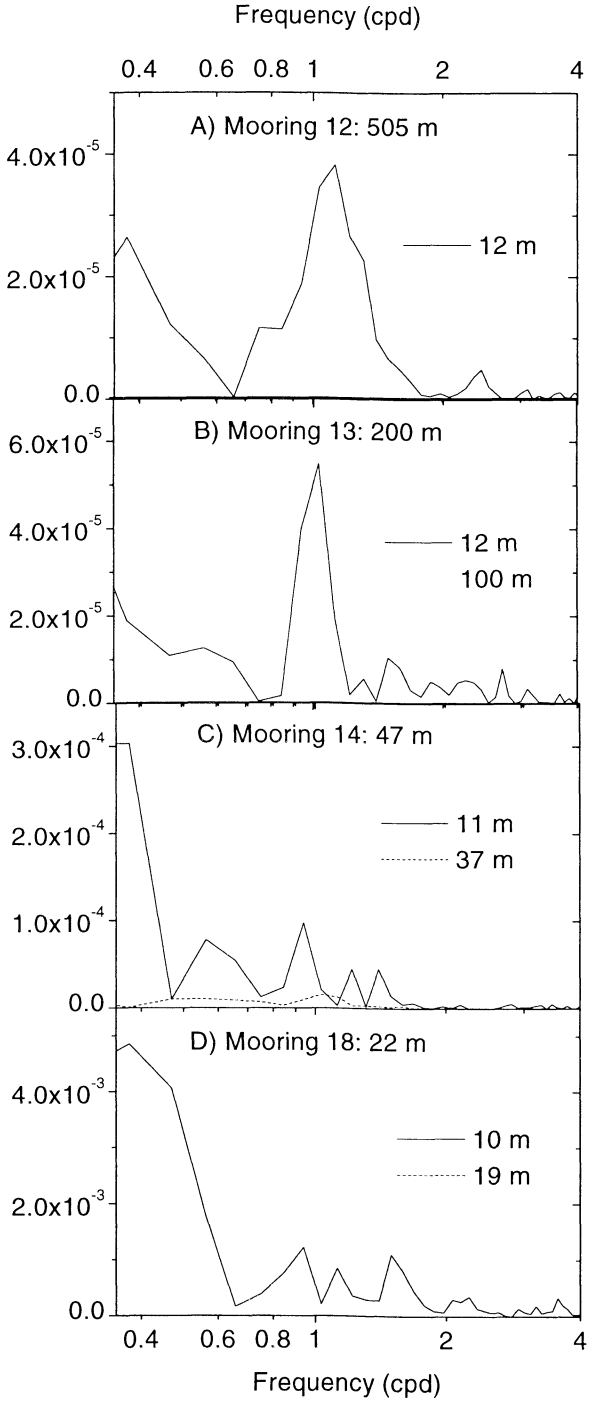

Figure 8. Power spectra of observed salinity time series at LATEX moorings. See Figure 1 for location. Units are $(psu)^2$.

5d) contains a transient signal like the one at mooring 14 but without a net increase in temperature. Neither meter has a strong near-inertial peak (Figure 6d). In fact, the spectra are biased to subinertial frequencies. There was a net cooling of the water column, possibly caused by local runoff or advection from offshore.

Using water level and temperature data, KG99 show that an internal Kelvin wave generated at the coast during downwelling could produce the transient temperature response observed on the shelf. This mechanism is discussed by *Csanady* [1984], *Millot and Crepon* [1981], and *Beletsky et al.* [1997]. Strong forcing such as that during a hurricane would produce a nonlinear wave with a steep front [*Bennett*, 1973], as observed at moorings 14 and 18.

2.3. Salinity

The observed near-surface salinity record (Figure 7a) at mooring 12 is similar to temperature but with less high-frequency variability (Figure 8a). There is a subinertial peak at 0.375 cpd, a broad near-inertial peak, and a smaller peak at 2.4375 cpd (period of 9.8 hours). The response is visible for only 2 days, however.

The salinity at the upper meter at mooring 13 (solid line in Figure 7b) oscillated by more than 1 practical salinity unit (psu) through JD 239, and remained relatively constant thereafter. This prestorm variability is reflected in the near-inertial peak (Figure 8b) at 1.03 cpd. This same frequency is present at the lower meter, although the amplitude of salinity variations is much smaller. The reduction in near-inertial oscillations after the storm suggests that the salinity gradient diminished because of turbulent mixing.

The surface salinity at mooring 14 (Figure 7c) increased by 3 psu on JD 238, followed by oscillations of less than 1 psu. This variability shows up as a power peak at 0.9375 cpd (solid line in Figure 8c) that may be tidally influenced. The salinity at the lower meter decreased slightly and oscillated weakly thereafter. This variability is represented by a near-inertial peak at 1.03 cpd in Figure 8c. The damping of this inertial motion at the surface meter may be associated with the transport of salty water from offshore within the mixed layer, as indicated by the higher salinity at the upper meter. A similar process is indicated at mooring 19 (not shown) but the resulting gradient was smaller.

The near-surface salinity at mooring 18 (Figure 7d) decreased by 4 psu on JD 235. This change had little to do with the approaching hurricane, however. There is no correlated temperature change either, and this may be caused by either instrument error or local advection processes. The spikes of low salinity after the storm are also problematical because of surface runoff and natural variability along the Louisiana shelf. The hypothesis that an internal Kelvin wave propagated westward on JD 239 is supported by a rapid decrease of 2 psu at the lower meter. This single peak is not accompanied by other oscillations or with a net change in salinity.

3. Simulating Internal Wave Generation With Realistic Topography and Forcing

The observations discussed in section 2 indicate that internal wave generation on the Louisiana continental shelf and slope was a complex process that extended beyond the available mooring arrays. The limited measurements prevent different generation mechanisms from being fully explored without the use of numerical models. Consequently, a numerical hindcast has been completed by using realistic forcing and bathymetry in order to resolve the interaction of the storm flow and the coastal topography better. It is not feasible to use this model to explain the detailed dynamical relationships between observations at the different moorings. Before proceeding to an analysis of internal wave generation, the model results will be compared with the observations to qualitatively determine how confident we can be in using them where measurements are lacking. The model will then be used to examine regional internal wave generation during the hurricane.

3.1. Princeton Ocean Model Hindcast

The wind and wave fields during Hurricane Andrew have been hindcast for 1000 UT August 24 to 0000 UT August 27. The 30-min wind fields are generated by first reanalyzing traditional cyclone parameters such as track and intensity (in terms of pressure). The more difficult storm parameters, such as the shape of the radial pressure field and the ambient pressure field within which

the storm is embedded, are then estimated. The time histories of these parameters are specified for the entire hindcast period. The storm track and storm parameters are then used to drive a numerical primitive equation model of the cyclone boundary layer [*Thompson and Cardone*, 1994]. The solution is compared with measured surface winds, and if necessary, the storm wind parameters are varied and the model rerun. This iterative procedure is continued to minimize error. The wind speed at Grand Isle (see Figure 1 for location) is consistently 3-4 m s^{-1} higher than measured but directions agree closely. Further details are available in C94.

The ocean circulation hindcast begins at 1000 UT August 24 with the ocean at rest and continues until 0000 UT August 31. Since no winds are available after 0000 UT August 27, the remainder of the hindcast has no atmospheric forcing. The winds were ramped up for 12 hours to reduce initial oscillations. The Louisiana continental shelf thus has a spin-up period of approximately 36 hours before hurricane winds are present.

This study uses the Princeton Ocean Model (POM) [see *Oey and Chen*, 1992; *Mellor*, 1993; *Mellor and Yamada*, 1982] to calculate three-dimensional baroclinic flows. The present choice of simulation parameters reflects the results of previous work on improving model skill for Hurricane Andrew [*Keen and Glenn*, 1998]. The model domain covers the Gulf of Mexico with a horizontal resolution of 0.05° (approximately 5000 m). A minimum water depth of 8 m is used with 50 σ levels and grid stretching near the surface. The resulting vertical resolution at the surface is 4 m for a maximum depth of 3656 m. The model equations are integrated by using an external time step (to solve for the barotropic flow) of 16.67 s and an internal time step (for baroclinic flow) of 304.44 s. Temperature and salinity profiles measured along the eastern mooring array (moorings 12 through 15) on August 24 were used to construct a depth-dependent temperature and salinity initial condition for the model [*Keen and Glenn,* 1998]. Wave-breaking turbulence is incorporated into the turbulence closure model by using the hindcast wave fields.

The inertial period for the northern Gulf of Mexico is between 24 and 26 hours. The dominant tidal periods in the Gulf of Mexico are the diurnal K_1 (23.9 hours) and O_1 (25.8 hours), which overlap

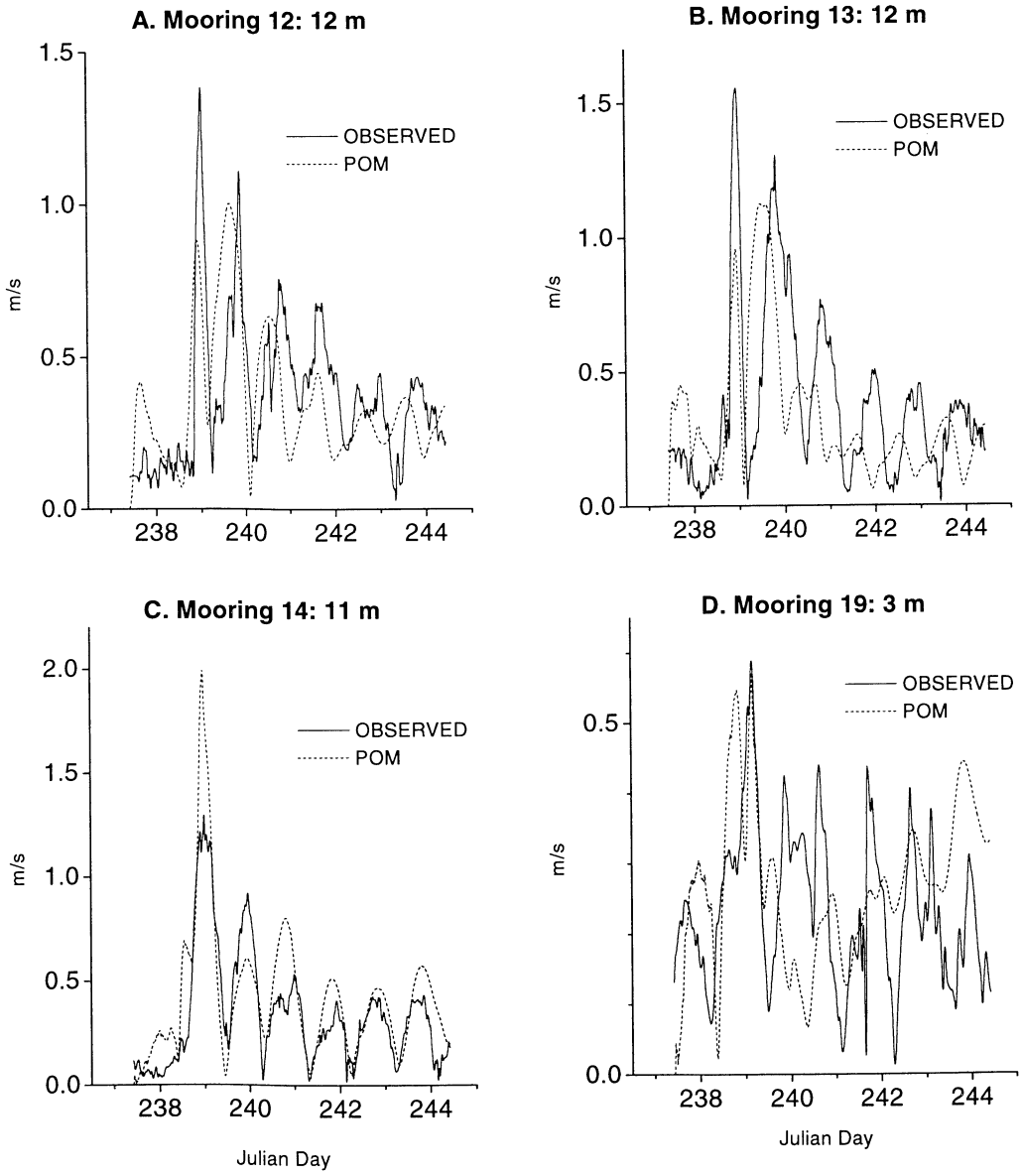

Figure 9. Time series of observed and POM-predicted current magnitudes at the upper meters at the LATEX moorings.

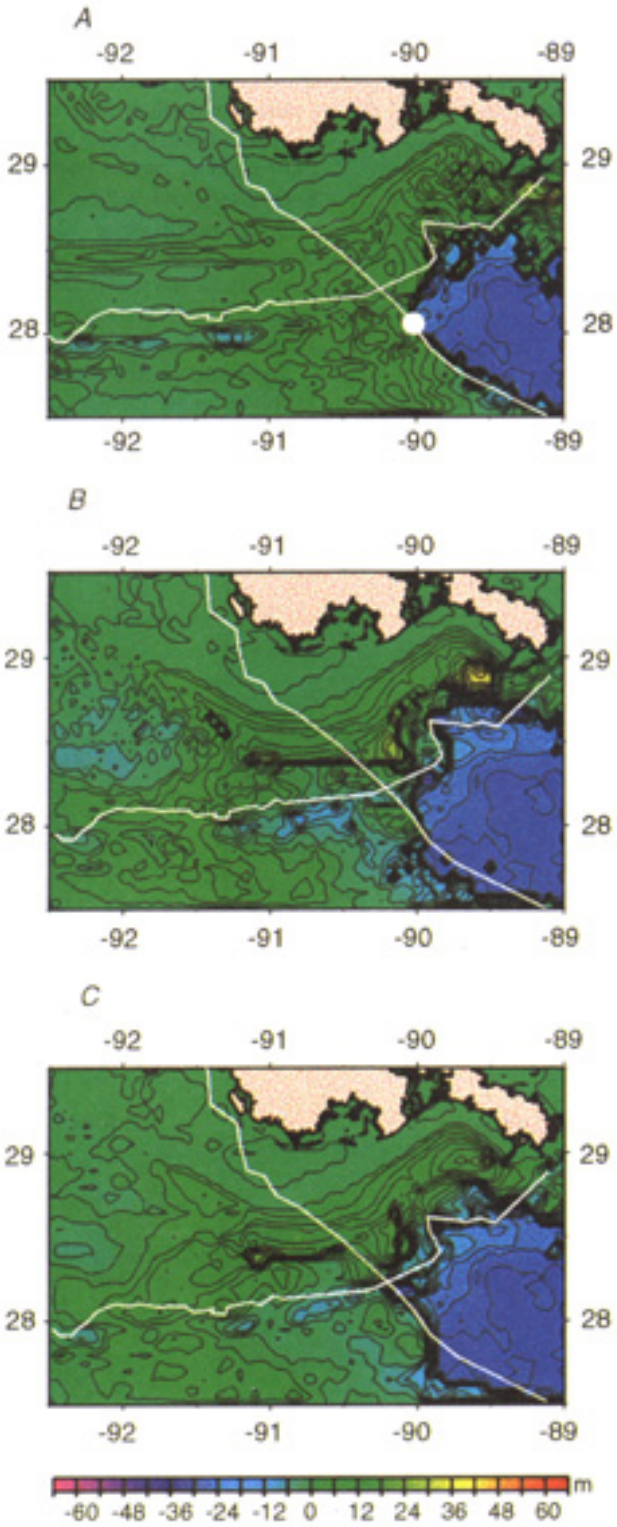

Plate 1. Model deviation (m) of the 26°C isotherm from its initial depth. The 200-m isobath is shown as well as the storm track and position of the eye. The eye was out of view in Plates 1a and 1c.

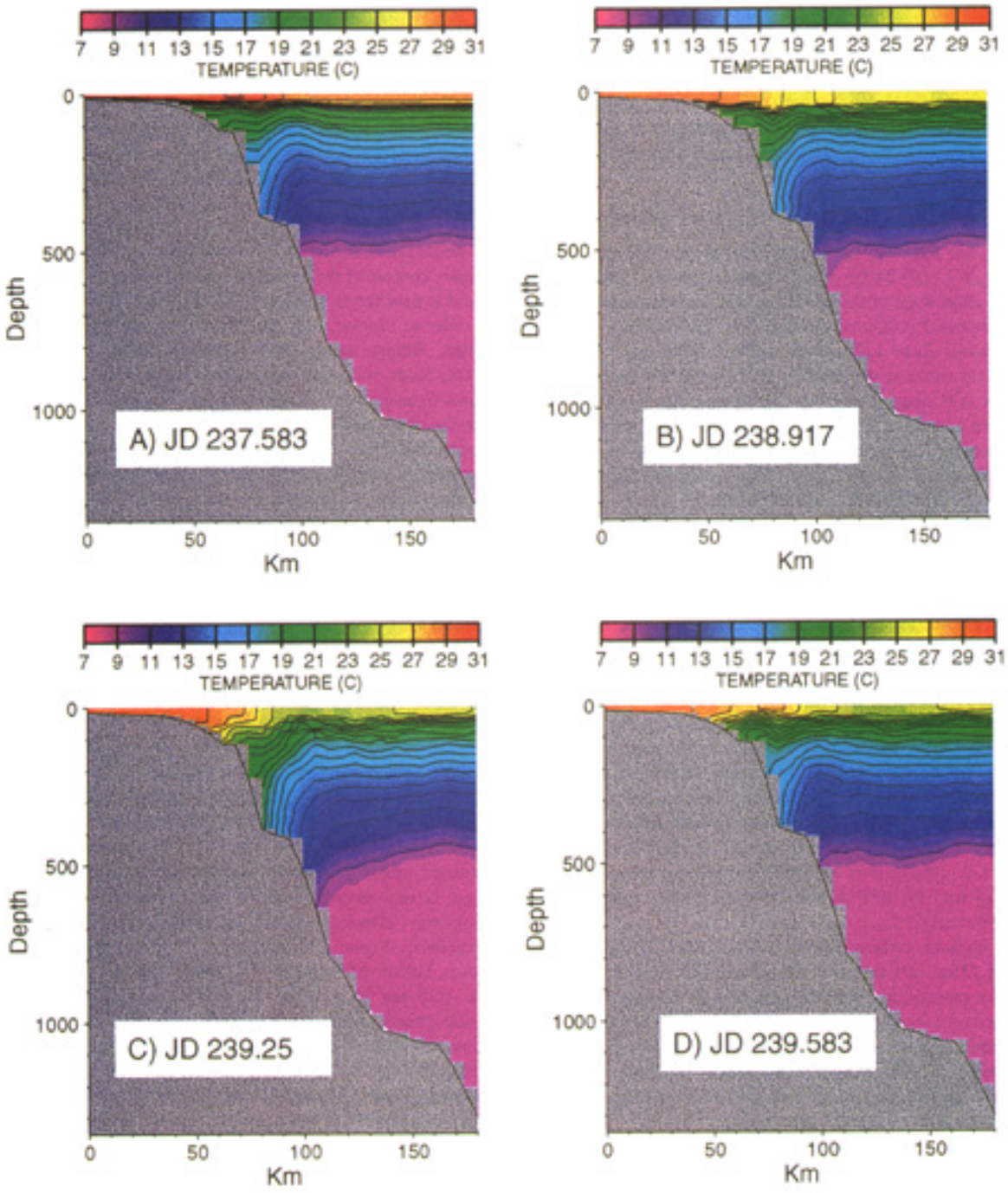

Plate 2. Cross sections of POM-predicted temperature along line AB from Figure 1.

the inertial period. Therefore tidal forcing is neglected in the simulation so that the inertial response can be evaluated more effectively.

During the spin-up interval, near-inertial oscillations were generated at the continental slope. The damping time for near-inertial oscillations in the model (see Figure 9) is more than 6 days, although this varies with location. However, this is not a significant measure of model stability because near-inertial oscillations are ubiquitous on this shelf. What is more important is that the magnitude of the prestorm currents is similar to the observations or small enough to be insignificant. Comparisons using a model with a spin-up interval of 5 days showed degradation in model skill, because of the lack of near-inertial oscillations prior to the storm.

3.2. Comparison of POM Results With Observations

The wind and wave fields used to force the POM end at 0000 UT August 27 (JD 240.0). Thus the model freely oscillates during the relaxation stage of the hurricane. One consequence is that the model-predicted posthurricane flow does not perfectly match the observations. *Keen and Glenn* [1996, 1998] use quantitative methods to examine the model's skill during the directly forced stage. A skill analysis based on the storm peak, however, is not applicable because of the nature of the observations; the storm peak is followed by free oscillations superimposed on coastal flows that are independent of the storm. This combined signal makes quantitative model skill analysis problematical. A qualitative comparison of the model-predicted and measured flows is made in KG99 and is not repeated here.

The purpose of this study is to examine internal wave generation. Therefore the most important index of model performance is in the frequency domain as discussed above. Thus this section will use the FFT method to compare the model's frequency response to the observations. As was demonstrated in section 2, the currents are more useful than temperature and salinity for examining internal waves because environmental factors not included in the model can significantly affect temperature and salinity. The robustness of the hindcast will be demonstrated by visually comparing the current magnitudes at several moorings. Before comparing the observations and model predictions, the observed current magnitudes were interpolated to the model times by using a polynomial interpolation [*Press et al.*, 1992]. However, the means were not removed prior to analyzing with the FFT in order to evaluate the model response more completely.

The hindcast surface currents (dashed lines in Figure 9a) at mooring 12 are very similar to the observations (solid lines) during the storm passage, but the peaks are low. A disparity in currents after the model winds ceased is apparent. The model predicts strong oscillations (Figure 10a) with a near-inertial peak matching the observations. A second near-inertial peak is predicted at a higher frequency but with less power than that observed. The model has more power at the subinertial frequencies.

The model-predicted surface currents at mooring 13 (Figure 9b) have low amplitudes and a slowly increasing phase error. The model spectrum (Figure 10b) is similar to the observations, but with a lower near-inertial peak and a strong subinertial peak. The phase error is caused by a shift of the near-inertial peak to a higher frequency. Note, however, that several superinertial peaks are predicted by the model.

The hindcast surface currents at mooring 14 (Figure 9c) have small phase errors, but the maximum current is 50% high. This behavior is explained by the power spectra (Figure 10c). The model has a near-inertial peak that almost exactly matches the observations. This peak is somewhat stronger, however. The subinertial peak is much larger as well. Several higher frequency peaks are absent in the observations at this mooring. The model results include these peaks with reduced amplitudes.

The hindcast surface currents at mooring 19 (Figure 9d) match the observations during the hurricane's passage but diverge significantly afterward. This behavior is probably due to the lack of wind forcing after the storm. The currents are out of phase by JD 240.0 because the near-inertial peak (Figure 10d) is very weak in the observations. The observations reveal a strong subinertial peak at 0.82 cpd (period of 29.2 hours). The model predicts a maximum peak at 0.586 cpd and a smaller peak at a near-inertial frequency. Note also the observed superinertial peak at 1.406 cpd (period of 17 hours), which is reduced in the model. The model does predict some of the higher-frequency motion, however.

This study focuses on mechanisms of internal wave generation. Therefore predicting temperature and salinity distributions is not a primary concern of the numerical hindcast effort. Nevertheless, it is useful to have the most accurate initial density distribution possible in order to capture local baroclinic processes in different water depths. Despite using depth-dependent initial temperature and salinity fields, we expect the model to predict less variability in the higher-frequency part of the spectrum because of local effects. In fact, the observed currents (Figure 10) do reveal more superinertial motion than that reproduced by the model. Local processes significantly affected the temperature and salinity distributions prior to the storm. Consequently, even when the most timely measurements were used, the observations were insufficient to generate three-dimensional fields that accurately reproduced the temperature and salinity records at all of the moorings. Furthermore, the inclusion of the tidal signal in the measurements makes a direct comparison between the model and the observations problematical. Other factors that prevent a quantitative comparison during the total study interval are local rainfall, runoff from the coast, and local heat fluxes. Because of these problems, a quantitative skill analysis cannot be applied to the model-predicted temperature and salinity results.

The depth-dependent initial condition for temperature and salinity used in the POM resulted in a thermal trend at mooring 12 (Figure 11a) that is opposite to the observed tendency. The model-predicted temperature in the mixed layer (dashed line in Figure 11) increased rather than decreased. Warmer water from the upper slope, as represented by 29.5°C water from mooring 13 (Figure 11b), was advected seaward by storm currents. The hindcast temperature (Figure 11b) at mooring 13 drops rapidly as the storm passes, before stabilizing at 2°C lower than the initial condition. The response at mooring 14 (Figure 11c) is similar to the measurements, with rapid mixing as the eye passed over. Subsequent near-inertial oscillations are seen in both measured and predicted time series. The model predictions at the western moorings (Figures 11d and 11e) are also similar to the observations. The discrepancies at moorings 12 and 13 are very likely partly attributable to an eddy because there is no analogous trend in the measured salinity time series (Figures 7a and 7b).

A direct comparison of the time series and power spectra of measured and predicted current magnitudes has been presented in this section. The results indicate that the POM is capturing the dominant baroclinic signals at the moorings. The model skill is greatest at the eastern moorings where the wind forcing was simplest and strongest. The response at the western moorings, which are located more than 2 R_w from the storm track, is not as good. The relaxation flow is well predicted by the model, despite the lack of poststorm wind forcing, because of the dominant near-

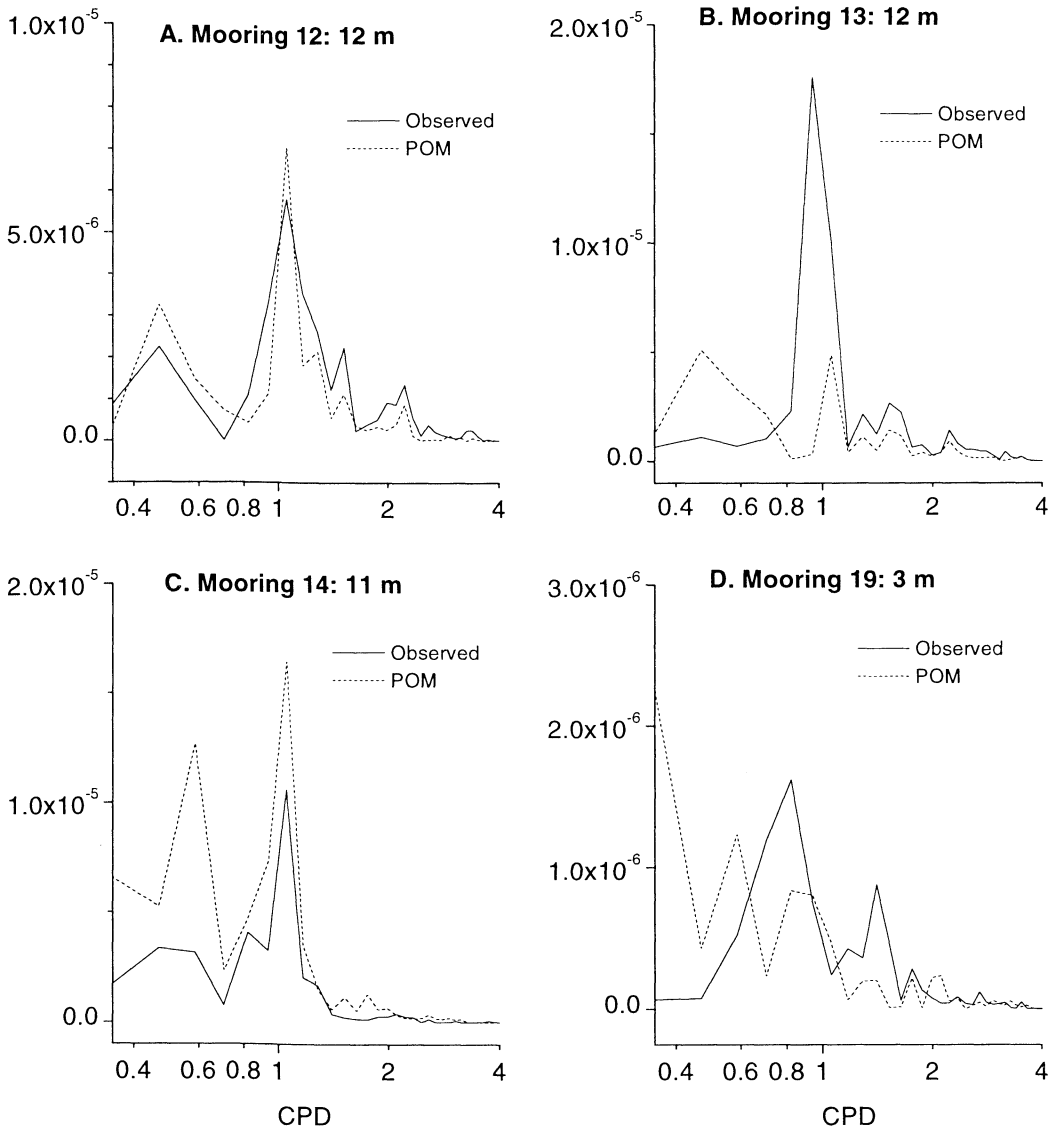

Figure 10. Power spectra of observed and POM-predicted current magnitudes at LATEX moorings. The vertical axis units are $m^2 s^{-1}$.

inertial and subinertial response of the shelf and slope waters. Higher-frequency motion is also reproduced, however. The greatest discrepancy is found in the subinertial range, where the model prediction is too large. This error is largest on the shelf west of the storm track. The model-predicted thermal history at the moorings is in general agreement with the observations on the shelf.

3.3. Baroclinic Flow on the Louisiana Shelf

The shallow-water currents on the Louisiana continental shelf during Hurricane Andrew have been discussed by KG99. The observations were used in combination with a numerical model to examine coastally trapped waves, near-inertial currents, and upwelling- and downwelling-favorable currents. However, KG99 focused on the buildup and directly forced stages only. In this study, we extend the analysis to the relaxation stage. A detailed examination of the baroclinic flow associated with internal waves during this interval has been completed in the frequency domain in sections 2 and 3.2. This section attempts to identify salient features of the three-dimensional current structure that accompanied the baroclinic oscillations seen in the measurements and the model.

The POM predicts surface flow to the northwest and parallel to isobaths near the Mississippi River delta as the hurricane eye crossed the continental slope (northeast corner of Figure 12a). This flow is part of a cyclonic eddy (labeled 1c in Figure 12a) driven by the wind stress. Bottom currents at this time (Figure 13a) are toward the shelf break and into Mississippi Canyon (see Figure 1 for location), forming a downwelling-favorable flow regime. Thus near-surface flow east of the canyon does not cross isobaths, whereas bottom flow crosses isobaths to within a few grid points of the coast. This flow is a significant deviation from previous reports of downwelling flows near canyons [*Klinck*, 1996; *Hickey*, 1997]. It is a geometric effect caused by the presence of the delta to the east. Flow on the western side of the canyon is more typical, with bottom currents following isobaths. Bottom currents are predominantly seaward within the canyon at this time. As was discussed by KG99, weak upwelling-favorable flow is present near the western moorings.

Just before landfall, a cyclonic barotropic eddy (labeled 2c in Figures 12b and 13b) is present at the head of the canyon, while flow on the shelf follows isobaths. This flow pattern is similar to

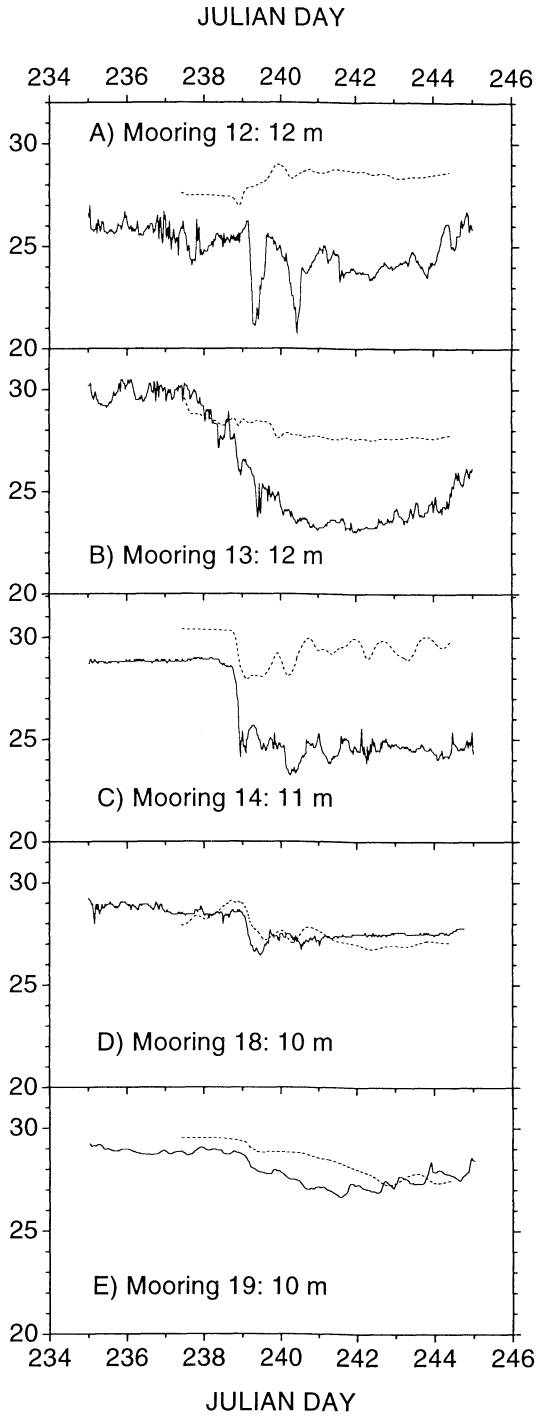

Figure 11. Time series of observed (solid line) and POM-predicted (dashed line) temperature (in degrees Celsius) at upper meters at LATEX moorings.

that for a narrow canyon [*Allen*, 1996]. There is also evidence of an anticyclonic eddy at the bottom (labeled 3a in Figure 13b). The surface expression of this weak gyre is masked by the wind-driven currents, however, as indicated by the dashed line used for eddy 3a in Figure 12b. Paired eddies near canyons similar to these have been observed in laboratory experiments during strong oscillatory flows [*Perénne et al.*, 1997]. The model-predicted eddies may be generated by combined inertial and wind-driven oscillatory flow on the outer shelf, where the wind has the same sense of anticyclonic rotation as the inertial flow. The upwelling-favorable flow west of the storm track continues at this time. The barotropic anticyclonic eddy labeled 4a is coupled to the cyclonic eddy labeled 5c. Eddy pairs such as this pair are generated through the interaction of the

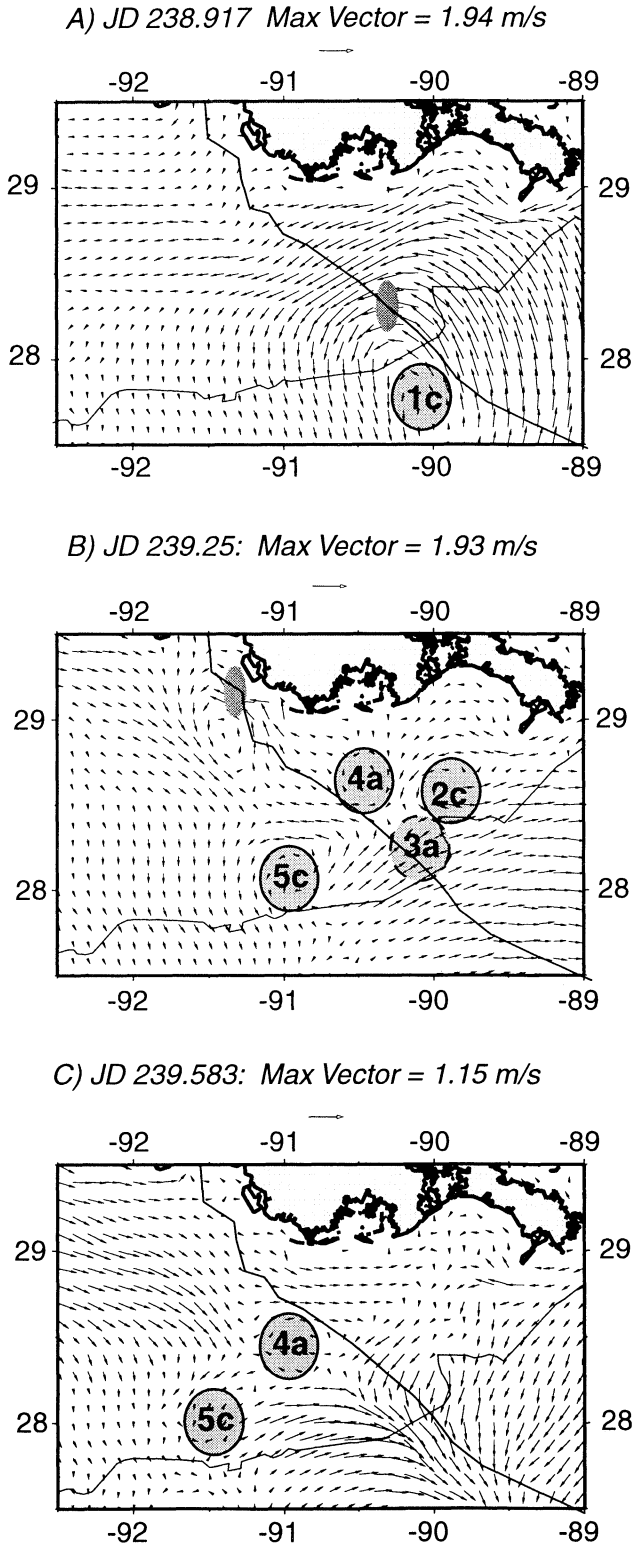

Figure 12. Snapshots of surface currents predicted by POM. The labeled circles are eddies referred to in text: a, anticyclone; c, cyclone. See text for explanation.

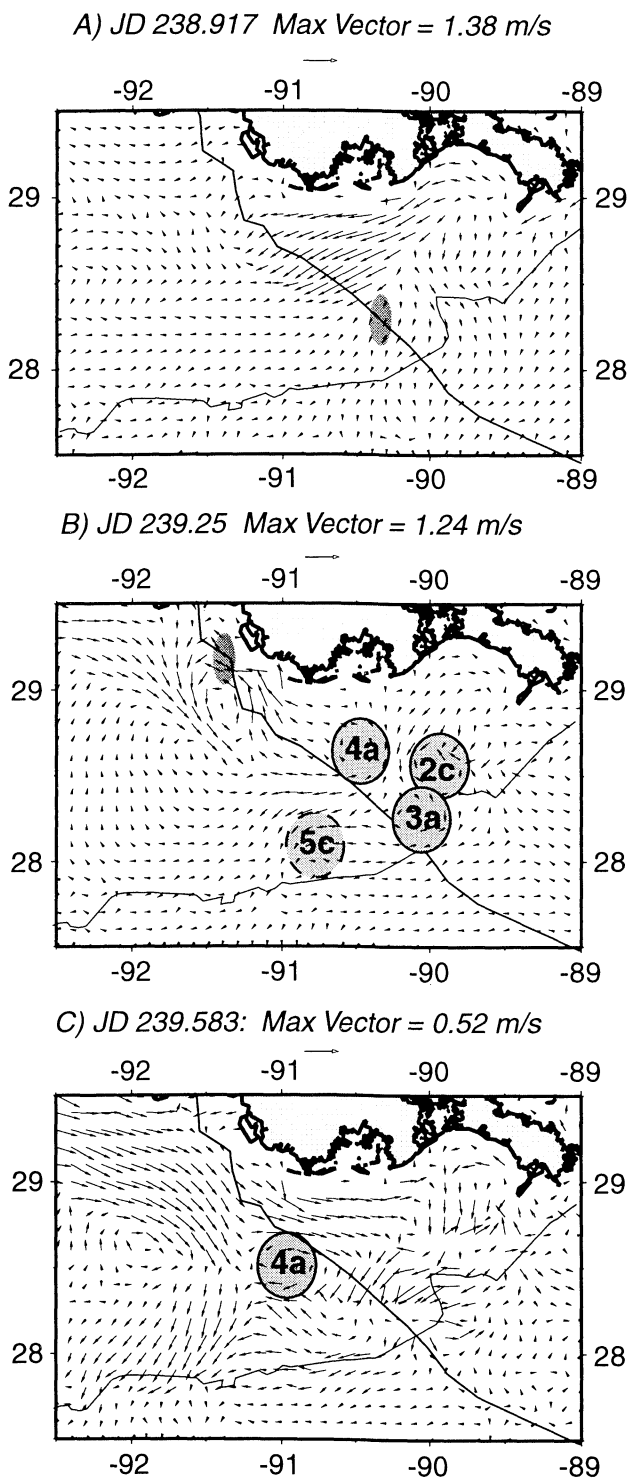

Figure 13. Snapshots of bottom currents predicted by POM. The labeled circles are eddies referred to in text: a, anticyclone; c, cyclone. See text for explanation.

large cyclonic eddy (1c in Figure 12a) with the bottom [*Fandry and Steedman*, 1994].

The wind weakened substantially after the eye made landfall and the relaxation stage began. The coupled eddy pair 4a-5c (Figure 12c) has propagated westward, and eddy 5c is no longer visible below the mixed layer (Figure 13c). Flow is barotropic on the inner shelf on the western side of the storm track, but upwelling-favorable currents persist at midshelf. Bottom currents are variable near the shelf break, but strong flow both to the east and to the west from the canyon is evident.

This discussion shows several characteristics of the storm flow that impact the generation of internal waves. First, the flow is strongly rotational. Much of this energy occurs at near-inertial frequencies. Eddies predicted by the model are generated by mechanisms that have been studied in field, laboratory, and modeling studies. The complex topography of the Louisiana shelf simply places these mechanisms in proximity to one another. Baroclinic oscillations are seen in both the open shelf setting to the west of the storm track and in the environment of Mississippi Canyon. A strong barotropic flow dominates on the inner shelf. These currents reverse direction after landfall. The barotropic Kelvin wave that drives this flow is not the topic of this paper. Nor do we pursue the continental shelf waves that also contribute to subinertial barotropic flow. Instead, the remainder of this paper focuses on near-inertial and superinertial internal wave generation due to thermocline displacement on the open shelf and within the canyon.

3.4. Thermocline Displacement

The generation of internal waves at the thermocline can be examined by using the predicted deviation of the 26°C isotherm (Plate 1) from its initial depth of approximately 35 m. Positive anomalies indicate downward deflection of the isotherm. When the hurricane eye was approaching the continental shelf (Plate 1a), downwelling was occurring near Mississippi Canyon where the 26°C isotherm was displaced downward by as much as 35 m. The possible cause of the variations in the isotherm anomaly along the shelf break will be discussed in section 4.2. There are both landward and seaward propagating internal waves superimposed on trapped coastal waves. These waves were generated during spin-up of the model. However, these modes are also generated by the storm, as will be discussed in section 4.

A baroclinic front located at 91°W is the result of thermocline deepening. This front subsequently propagates westward as a trapped coastal wave (Plates 1b and 1c), which follows the inner shelf topography rather than the continental slope. This transient wave appears to be an internal Kelvin wave as proposed by KG99. However, the estimated frontal speed of 0.7 m s^{-1} is significantly less than the value of 4 m s^{-1} estimated from the observations. This kind of discrepancy between model-predicted and observed internal fronts has been noted by *Beletsky et al.* [1997] for internal Kelvin waves in Lake Michigan. Among the possible causes are numerical dispersion, errors in stratification, heat and salt fluxes, bathymetry errors, and wind forcing.

Several hours after the eye made landfall (Plate 1b), the 26°C isotherm anomaly indicates that multiple internal waves are being predicted by the model. Superinertial edge waves are propagating along the 200-m isobath, after being generated near Mississippi Canyon. These edge waves have a wavelength similar to the storm R_w. A near-inertial wave is generated west of the canyon. This wave originates at the large positive anomalies near 90.1°W, between the storm track and the 200-m isobath. It is seen as a large 26°C anomaly gradient landward of the 200-m depth contour. Note the similarity of this wave in Plate 1c, which is 24 hours later. There is also evidence of internal waves within the canyon. Subsequent internal wave generation consists of shelf waves propagating to the west and oscillations within the canyon. The near-inertial waves generated at the slope, which are not apparent in these plots, will be discussed in section 4.

3.5. Internal Waves Within Mississippi Canyon

Displacement of the thermocline was important for generating internal waves during Hurricane Andrew. The largest anomalies in the depth of the 26°C isotherm are predicted by POM near Mississippi Canyon because of downwelling into the canyon prior to landfall. Furthermore, eddies near the canyon influenced the generation and propagation of near-inertial waves observed at the moorings. Because of the lack of observations within Mississippi Canyon, however, it is necessary to rely on the numerical model to examine internal wave processes in this area. The model does not predict the currents, temperature, and salinity exactly. Nevertheless, it accurately reproduces the overall spatial and temporal evolution of the storm response. Thus it can be used to examine the generation of internal waves with frequencies of 0.7 to 2 cpd in areas where observations are lacking.

Mississippi Canyon is approximately 30 km wide at the 200-m isobath (see Figure 1). Thus it is significantly larger than typical canyons discussed in the literature. For example, Juan de Fuca Canyon [*Cannon,* 1972], Hudson Canyon [*Hotchkiss and Wunsch,* 1982], and Grand Rhône Canyon [*Durrieu de Madron,* 1994] are between 10 and 15 km wide. Astoria Canyon [*Hickey*, 1997] and Monterey Canyon [*Petruncio*, 1996] are less than 10 km in width. The internal deformation radius $R_0 = N h f^{-1}$ (where h is the depth) for Mississippi Canyon is approximately 36 km, which is of the same order as the canyon width. Consequently, the surface currents in Figure 12 are similar to *Klinck*'s [1996] weakly stratified case (i.e., wide canyon). Bottom currents (Figure 13a) indicate downwelling on the upstream margin of the canyon as the storm approached. Upwelling subsequently begins on the upstream side of the canyon (Figure 13b) and spreads to the downstream margin after landfall (Figure 13c). This flow is in general agreement with the results of previous model studies [*Allen*, 1996; *Chen and Allen*, 1996], but for downwelling- rather than upwelling-favorable winds. This general similarity extends to the generation of eddies discussed above.

The generation of internal waves within Mississippi Canyon can be examined by using cross sections along the canyon axis (see Figure 1b for location). The initial temperature (Plate 2a) distribution was generated by using hydrographic data from the eastern mooring array. Warm water from the shelf is found on the slope at depths of 400 m. Deepening of the mixed layer occurs as the storm intensifies (Plate 2b), with maximum downward deflection of the thermocline at a distance of 80 km from the canyon head. This downwelling peaked just before the eye made landfall (Plate 2c). At this time, warm water from the inner shelf has penetrated to a depth of 100 m within the canyon, and the 18°C isotherm has been depressed from 150 m to 400 m. This downwarping pushed the 8°C isotherm to a depth of 650 m. After landfall (Plate 2d), the isotherms have rebounded to near their original depth, and an internal wave with a wavelength of 50 km is seen along the 8°C isotherm.

Internal waves within Mississippi Canyon can be identified by using phase plots of currents from the lowest sigma levels from the POM model (Plate 3). The currents in the figure have been rotated to align with the canyon axis. In addition, the magnitudes at each station along the canyon have been normalized separately. This method focuses on the variability at each station without biasing the result with the largest magnitudes, which occur near the canyon head. Negative values of across-axis and along-axis currents indicate flow to the southwest and southeast, respectively. Maximum bottom currents are predicted at JD 239 (0000 UT August 26) throughout the canyon. Axial flow was seaward within the main canyon, at distances between 50 and 150 km. This reflects the generation of downwelling currents along the eastern canyon margin rather than near the canyon head, where flow was primarily parallel to depth contours. After the initial pulse, the currents are dominantly inertial. However, there is evidence in the crosscurrents (positive values in Plate 3a) of a wave propagating seaward at approximately 0.5 m s^{-1}. It is also seen in the axis currents although it is masked by the large variations at near-inertial frequencies. This phase appears to exit the canyon.

The previous discussion of temperature and currents within Mississippi Canyon demonstrates that different internal waves were being generated in this area. However, the complexity of the realistic topography, wind, and stratification in the POM hindcast makes it difficult to separate the wave phases generated during the hurricane. In order to isolate the internal waves, it is useful to simplify the problem, especially to eliminate the subinertial frequency continental shelf waves associated with the spatial variability of the wind field.

4. Simulating Internal Wave Generation Over Idealized Topography

The purpose of using a simplified model in the present study is to isolate the mechanisms for generating internal waves on the continental shelf and slope, especially in Mississippi Canyon. The results from the POM indicate that this feature is a significant site of wave generation. The observations indirectly support this conclusion, although direct measurements are not available. Idealized models can be used to examine physical mechanisms for wave generation without the complexities introduced by continuous stratification, spatially variable wind stresses, and topographic irregularities. However, it is important that the simplifying assumptions do not invalidate their use.

The water column on the continental shelf and slope prior to Hurricane Andrew can be approximated as a two-layer system. As is shown by Plates 1 and 2, internal waves are generated at the thermocline by the wind. These oscillations are readily studied by using an isopycnal model [e.g., *Cooper and Thompson*, 1989]. Internal waves generated by topography commonly travel as beams close to the generation region [*Petruncio*, 1998]. Farther away, these waves also tend toward a mode 1 baroclinic structure. Idealized models have proven useful to examine the interaction of stratified shelf and slope flows with topography [e.g., *Allen*, 1996; *Carrasco*, 1998]. Thus it is advantageous to simulate internal wave generation during Hurricane Andrew by using a two-layer isopycnal numerical model.

4.1. Shallow Water Model

The Shallow Water Model (SWM) [*Allen*, 1996] as used in this study consists of two-layers. It incorporates an enstrophy- and energy-conserving formulation for the advection and Coriolis terms [*Arakawa and Lamb*, 1981], except where the depth of a layer becomes very small. When this occurs, the model uses the first-order upwind scheme for the mass conservation equation. The vertical viscosity takes the form of a linear drag between the two layers and a linear Ekman-type bottom drag at an angle of 20° on the bottom layer. Because of the shallow water (minimum depth of 30 m) used in the simulation, a moderately large vertical viscosity had to be used to keep the model stable. Parameters used in the simulation are given in Table 2.

The model grid (Figure 14a) contains a straight coastline, shelf, and slope with a width similar to the study area. The slope is cut by

Table 2. Parameters Used in the Shallow Water Model

Parameter	Value
Grid size	3 km × 3 km
Domain size	600 km × 600 km
Upper layer depth	20 m
Reduced gravity	0.038 m s^{-2}
Horizontal eddy viscosity	500 $m^2 s^{-1}$
Vertical eddy viscosity	0.05 $m^2 s^{-1}$
Ekman layer depth	14 m
Coriolis parameter	6.83×10^{-5} s^{-1}
Beta	0
Northern boundary	30 m deep, no slip
Southern boundary	1000 m deep, zero gradient velocity, constant gradient surface and interface
East/west boundaries	periodic plus 40 grid point sponge to no east/west variations
Time step	10 s
Total simulation	4 days

a canyon similar in scale to Mississippi Canyon. This simple topography reduces alongshore variations in the flow field and permits the flow interaction with the canyon to be examined in detail. This simulation considers the effect of a spatially uniform wind stress (Figure 14b) with magnitudes and time dependence representative of mooring 14, which lay directly along the storm track. The idealized model eliminates the effects of spatially variable winds and continuous stratification. A uniform wind stress

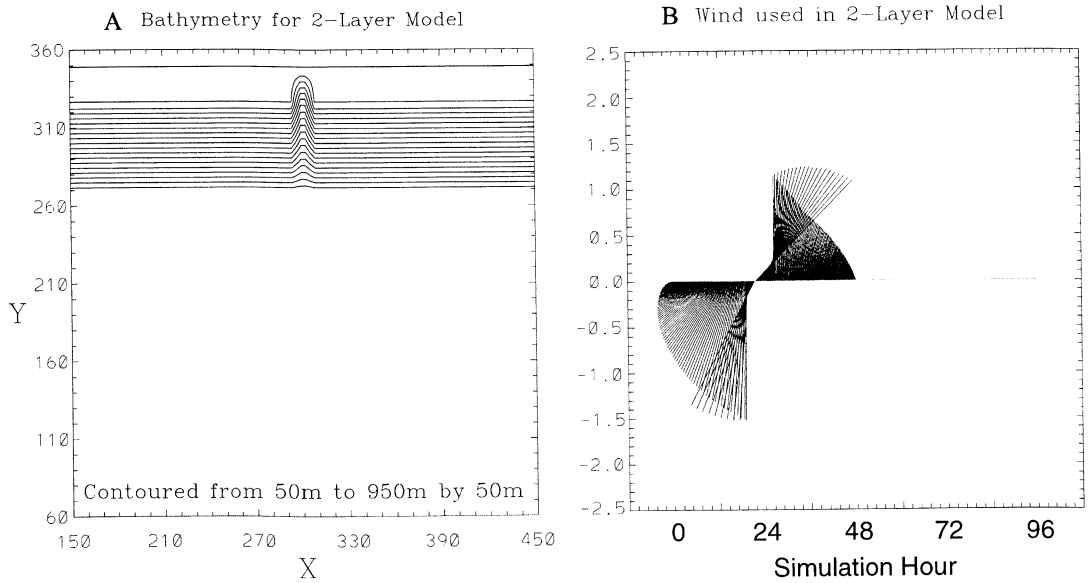

Figure 14. (a) Bathymetry used for Shallow Water Model simulation. Units are kilometers. (b) Time series of uniform wind stress used in SWM simulations. Units are $m^2 s^{-2}$ (stress/water density).

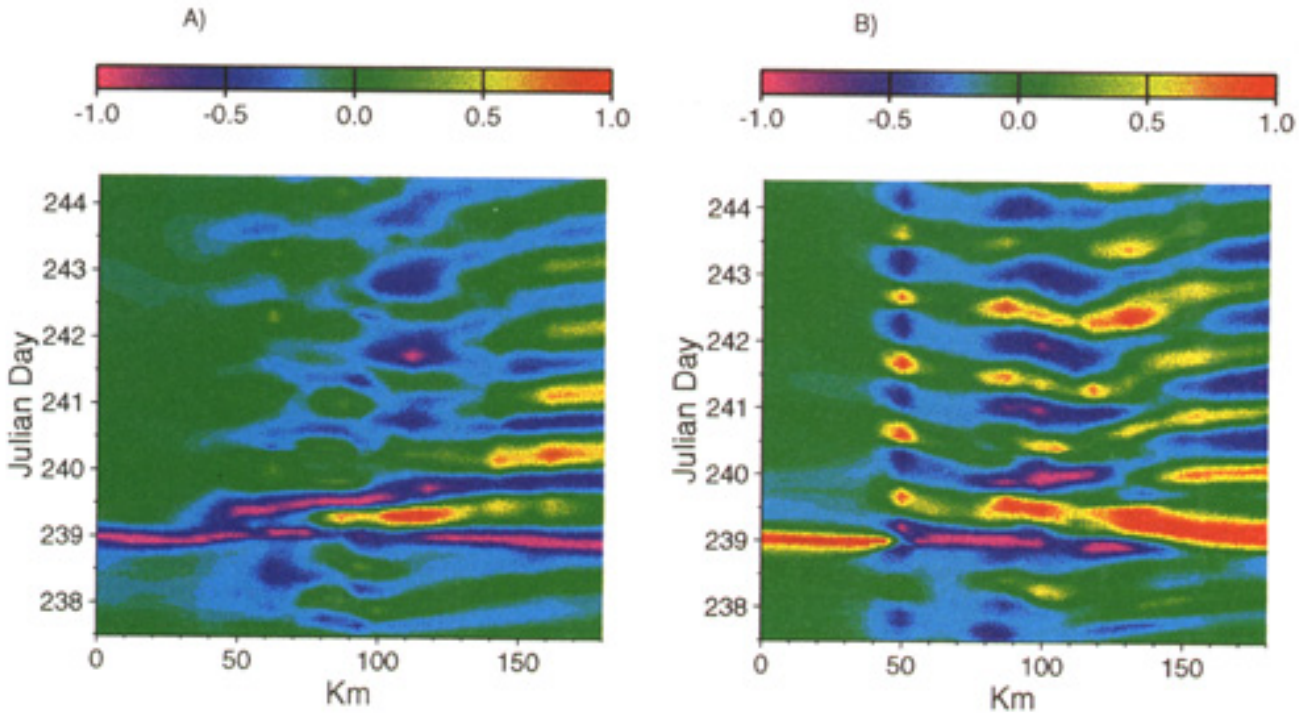

Plate 3. Phase plots of normalized (a) cross-canyon currents and (b) along-canyon currents. The cross section is line AB in Figure 1.

will not generate continental shelf waves, which would obscure lower-amplitude waves that cannot be identified from the observations. The simple stratification precludes higher-mode internal waves. The idealized model simulation is not intended as a hindcast of Hurricane Andrew. This model is useful to examine fundamental processes only, and thus no attempt is made to validate or tune the SWM. The use of dates in describing the SWM results is for convenience only.

4.2. Model Results

The response of the simplified model to the storm winds includes surface velocities as high as 2 m s^{-1} and a coastal storm surge of 0.32 m. Upwelling predicted during day 1 produces interface elevations of 6 m. Subsequent downwelling lowers the interface by as much as 31 m. The internal waves generated by the SWM are of particular interest to the present study. Since the idealized wind forcing is spatially uniform, the SWM does not generate the subinertial shelf waves discussed by *Tang and Grimshaw* [1995]. The SWM generates coastally trapped waves, however, because of the presence of the canyon.

4.2.1. Near-inertial oscillations. The inertial response in the deep ocean consists of a baroclinic oscillation with velocities of 1.5 m s^{-1} in the upper layer (not shown). This oscillation decays to 1 m s^{-1} during the following 2 days. This primarily first-mode, deepwater oscillation generates flow at the same frequency over the slope and shelf. The SWM-predicted near-inertial oscillation is seen in the interface height (Figure 15) on the slope (water depth similar to mooring 12), which has a maximum downward displacement of 8 m at 12 hours after the peak wind. The observed mixed-layer temperature at mooring 12 (Figure 5a) increased by 1°C during the local peak winds. The subsequent decrease of 5°C represents an upward movement of approximately 30 m (see Figure 2). This deflection can only be estimated, however, because the actual temperature profile was not measured during the storm. The precise lag in timing of the response at mooring 12 cannot be determined either, because the wind was not measured. Nevertheless, by using the hindcast wind (C94) and the measured temperature, the lag between the peak wind and maximum downward deflection is estimated to be 10 hours. The SWM predicts an interface rebound of 12 m, which is less than half the estimated rebound, but the lag error (relative to the peak wind) is only 2 hours. The usefulness of this comparison is in demonstrating that the response on the slope is dominantly inertial, which is to first order captured by the idealized SWM.

4.2.2. Trapped edge waves. The canyon in the model topography generates superinertial edge waves over the shelf. This is the major barotropic response to the canyon in SWM. These waves have a period of 100 min and a wavelength of about 340 km. The maximum amplitude of 0.18 m occurs at model day 1.5 (JD 239.0). They are generated when surges within the canyon reach the coast. These waves travel both eastward and westward from the canyon, with the expected mode splitting and faster propagation to the east [*Fandry and Steedman*, 1994; *Tang and Grimshaw*, 1995]. The velocity associated with this wave turns cyclonically in the simulation, partly because of the large value of the bottom drag required for numerical stability. These high-frequency waves are barely resolved by the observations and the POM results.

4.2.3. Internal waves. The results from the POM (Plate 1) show a persistent ridge in the 26°C isotherm over the continental slope. Internal waves propagate both landward and seaward away from this feature. This process is most apparent during the POM spin-up interval, before the storm generates other baroclinic oscillations. Because of the simpler topography, stratification, and wind field used in the idealized model, these internal waves can be analyzed in detail with SWM.

The SWM results show that interaction of the near-inertial oscillations with the continental slope is the dominant generating mechanism for the internal waves over the slope and shelf. An initial trough in the interface height (Figure 16) forms at the shelf break (Y = 310 km) when the flow is westward over the shelf and

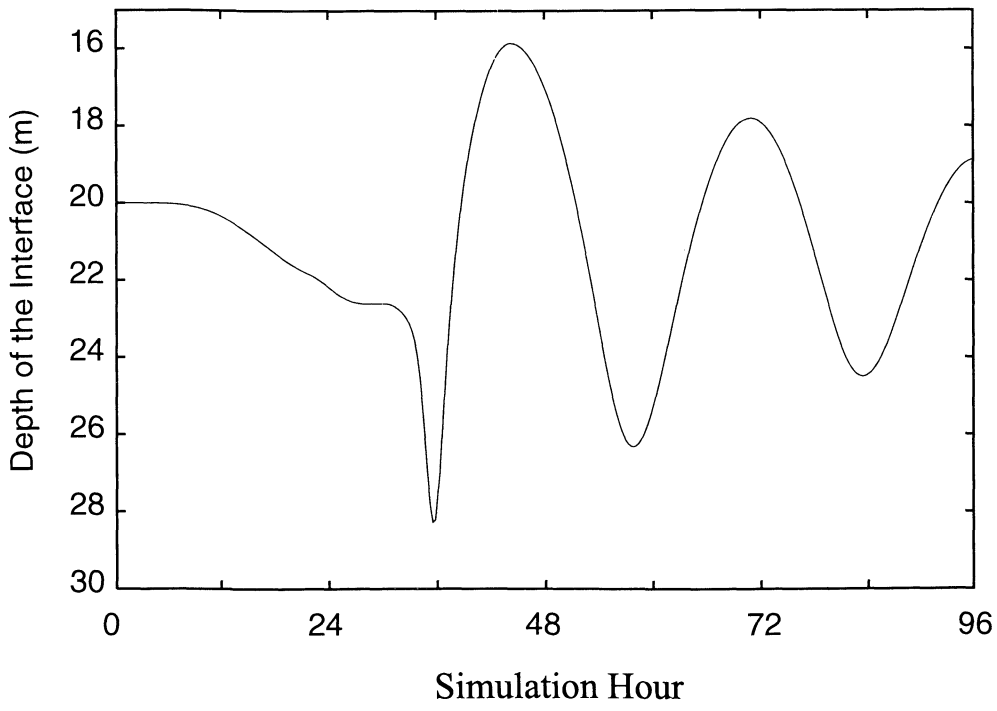

Figure 15. Time series of interface depth on the continental slope calculated by the SWM.

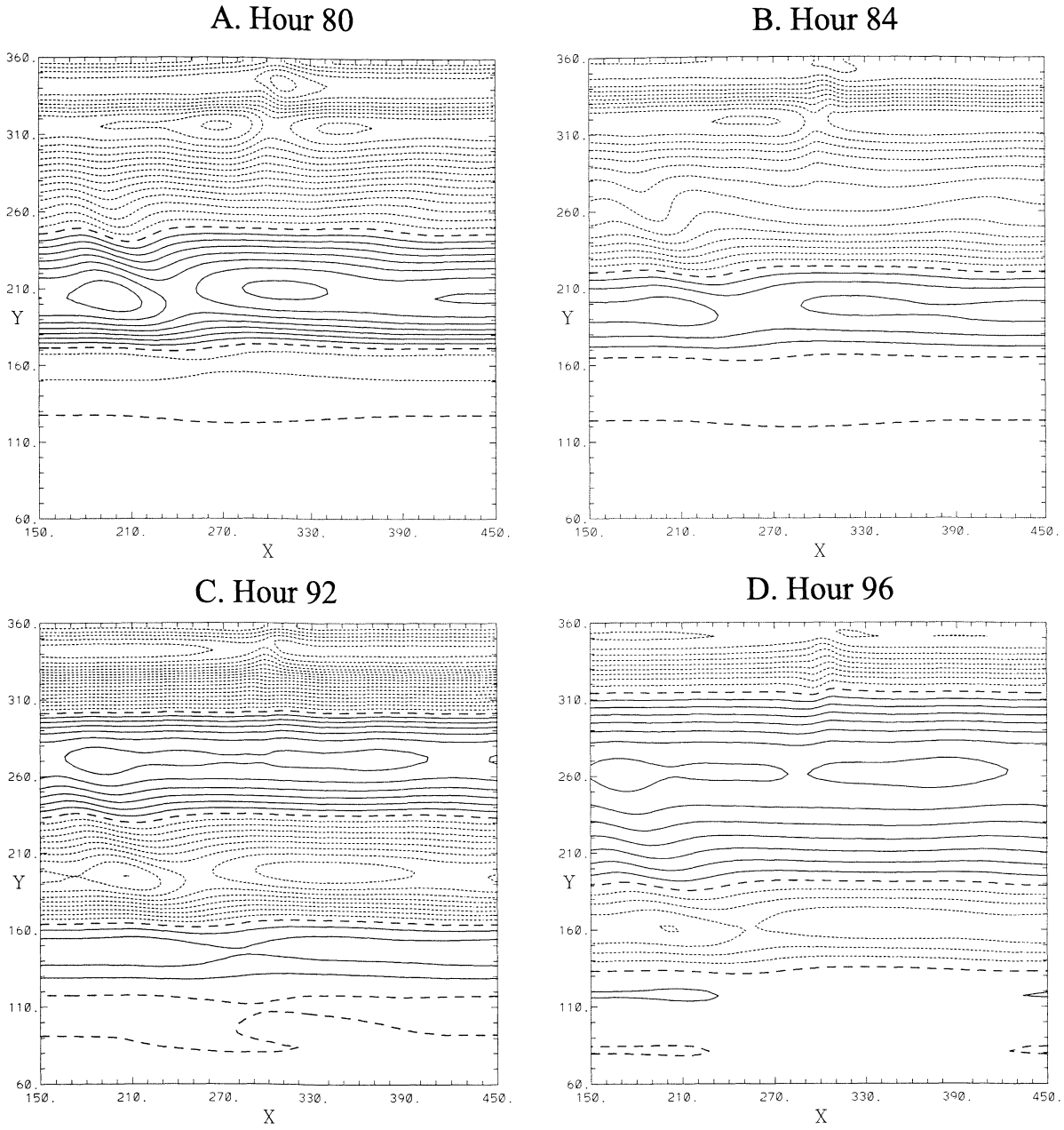

Figure 16. Interface height computed by SWM at (a) 32 hours after wind stopped, contoured from -3.75 m to 1.75 m by 0.25 m, (b) 36 hours after wind stopped, contoured from -5.8 m to 1.2 m by 0.4 m, (c) 44 hours after wind stopped, contoured from -4 m to 1.5 m by 0.25 m, and (d) 48 hours after wind stopped, contoured from -3.6 m to 2.8 m by 0.4 m. The solid lines are positive, the dashed line is the zero contour, and dotted lines are negative contours. Note that the wind was stopped at hour 48.

southwestward in deep water. This divergent flow is seen in the POM results for surface and bottom currents as the storm approaches (Figures 12a and 13a). The trough subsequently divides (Figure 16b), with one wave traveling shoreward (Y = 320 km) and the other traveling seaward (Y = 260 km). The shoreward propagating wave has a phase speed of 0.8 m s^{-1}. The offshore wave travels at a phase speed of 1.9 m s^{-1} with a group speed of 0.7 m s^{-1}.

It is important to note that the idealized model does not predict the regional response of the Louisiana shelf and slope to the hurricane. The internal waves are generated only where the deepwater storm flow interacts with topography. As is suggested by the POM results, this generation mechanism would operate primarily between 90°W and 92°W, a distance of less than 200 km. However, this length is significantly larger than the storm scale R_w, which is 40 km; thus the strong oscillations at mooring 19 (Figure 10d).

The uniform westward flow along the shelf and slope associated with the deepwater inertial oscillation generates a waveform with its crest located over the center of the slope at Y = 270 km (Figure 16c). The crest propagates seaward at a phase speed of about 1.2 m s^{-1} as an internal wave. However, it does not split (Figure 16d) and is somewhat broader than the seaward traveling trough discussed above. It has about one-half the amplitude. This wave cannot be identified in the complex results from POM or in the observations.

4.2.4. Poincaré waves. Downwelling into Mississippi Canyon depresses the interface depth in the SWM, just as the 26°C isotherm flexes downward in POM. After the wind stress is removed, the interface relaxes and generates a transient flow within the canyon. The wave front associated with this flow propagates seaward as a Poincaré wave, followed by an oscillatory tail due to dispersion [*Gill*, 1982]. Eliminating the internal waves generated over the slope reveals these waves in the SWM results. Since the internal waves are parallel to the isobaths for the simple model bathymetry, the interface height far from the canyon, but at the same Y location, can be subtracted at every grid point. The result is a map of interface dislocations associated with the Poincaré waves only (Figure 17).

The Poincaré waves travel seaward along the canyon axis at about 0.5 m s^{-1}. After exiting the canyon, the crests and troughs are advected to the west by the near-inertial oscillations discussed above, producing a scalloped path. The group velocity of these waves is estimated to be 0.5 to 0.7 m s^{-1}, at 15°-25° west of directly offshore. The phase velocity is approximately 1 m s^{-1}, at 25°-45° west of directly offshore. The maximum amplitude of the interface deviation of the waves decreases from 1 m to 0.5 m during the 2.5 days after the wind ceases.

The idealized model demonstrates three mechanisms for isopycnal displacements during Hurricane Andrew: (1) near-inertial oscillations in deep water are generated directly by the wind field, (2) internal waves parallel to the shelf break are produced by the interaction of deepwater inertial flow with the continental slope, and (3) a transient wave is generated in Mississippi Canyon by the strong up- and down-canyon flows directly forced by the hurricane. The waves induced within the canyon disperse after exiting the canyon and lose amplitude. It is unlikely, therefore, that they contribute to the oscillations observed at the moorings, which are probably due to the other mechanisms. The second mechanism differs subtly from the internal tide generation described by *Holloway* [1996], because baroclinic rather than barotropic currents force it.

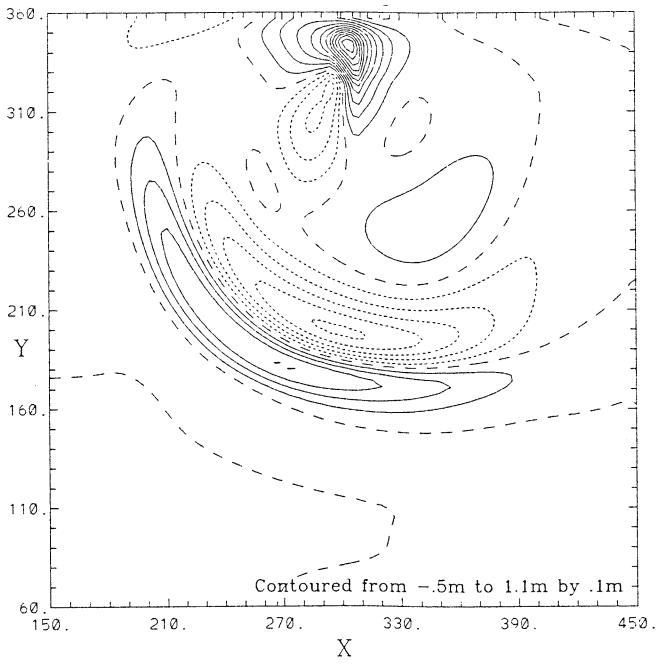

Figure 17. Normalized interface variation predicted by the SWM at hour 72. The Poincaré waves generated in the canyon during the storm passage are visible as a curved crest and trough in the middle of the figure. See text for explanation.

5. Discussion and Summary

Observed currents, temperature, and salinity from moored instruments on the Louisiana continental slope and shelf reveal multiple baroclinic oscillations during Hurricane Andrew. In addition to turbulent mixing, the current meters near the storm track recorded internal waves that were dominantly near inertial on the shelf and slope. A barotropic subinertial signal also indicates that continental shelf waves were generated near the storm track. More than 2 R_w west of the track, the response was dominantly subinertial. Superinertial internal waves were also present. These measurements are supplemented by numerical models in order to identify possible internal wave generation mechanisms in areas not covered by the observations.

The Princeton Ocean Model was run with realistic topography, stratification, and wind forcing. The model-predicted currents reveal power peaks at near-inertial and subinertial frequencies that match the observations. A comparison between model-predicted currents and temperature reveals the presence of significant variability in the observations that does not appear to be caused by local storm wind forcing. These effects include precipitation and runoff, internal waves and continental shelf waves originating before the storm and from other areas, deepwater flows such as eddies, and astronomical tides. Temperature and salinity measurements are especially sensitive to these factors.

The model predicts eddies generated by interaction of the storm flow with Mississippi Canyon. However, the development of these eddies differs substantially from previous reports [e.g., *Klinck*, 1996; *Allen*, 1996; *Hickey*, 1997], because of the highly rotational hurricane winds and the presence of the Mississippi River delta to the east. An examination of the depth anomaly for the 26°C isotherm shows that an internal wave front is a likely contributor to the observations at the western moorings. The model also shows the complex interaction of internal waves generated at the thermocline with the shelf topography. The thermocline anomaly, bottom currents in the canyon, and temperature within the canyon all reveal internal waves generated within the canyon. However, the complexity of the model predictions prevents the unequivocal identification of these waves.

A two-layer isopycnal model (SWM) [*Allen*, 1996] is used with idealized topography and spatially uniform winds to isolate internal waves generated in and around Mississippi Canyon. This model reproduces mode 1 baroclinic oscillations associated with the canyon and the continental shelf and slope only. The results are in agreement with the POM simulation, but there is significantly less noise. Internal waves generated over the shelf break in both models result from divergence of shelf and deepwater storm flows. These waves propagate seaward in both models. The SWM results also reveal a landward propagating phase and a second internal wave located over the slope, which propagates seaward. Along-axis flow within the canyon generates Poincaré waves in both models; the seaward propagation speed is predicted to be 0.5 m s^{-1} by both models. The interaction of these waves with the deepwater flow and other internal waves is revealed in the POM-predicted thermocline anomaly.

The combination of the observations and the results from the numerical models indicate several mechanisms for generating long internal waves: (1) near-inertial internal waves were generated across the slope and shelf by dislocation of the thermocline by the

wind stress; (2) interaction of inertial flow with topography generated internal waves along the shelf break, which bifurcated into landward and seaward propagating phases; (3) downwelling along the coast depressed the thermocline; after downwelling relaxes, an internal wave front propagates as a Kelvin wave; and (4) Poincaré waves generated within Mississippi canyon propagate seaward while being advected westward over the continental slope.

These processes interact to produce a three-dimensional internal wave field, which was only partly sampled by the observations. The use of numerical models with different characteristics has made it possible to identify individual internal wave generation mechanisms and examine their complex interaction. The prediction of several of these internal waves by both models supports the use of numerical models to assist in analyzing complex baroclinic flows in coastal regions. Because of this combined approach, this study shows that the baroclinic response to hurricanes in shallow water can be as important as the barotropic response.

Acknowledgments. The first author was funded under the Naval Research Laboratory Very High Resolution 4-D Coastal Ocean Currents project, Program Element 62435N of the Office of Naval Research. The second author was funded under the NSERC Research program. LATEX mooring data were supplied by the Minerals Management Service (MMS).

References

Allen, S. E., Topographically generated, subinertial flows within a finite length canyon, *J. Phys. Oceanogr.*, *26*, 1608-1632, 1996.

Arakawa, A., and V. R. Lamb, A potential energy and enstrophy conserving scheme for the shallow water equations, *Mon. Weather Rev.*, *109*, 18-36, 1981.

Beletsky, D., W. P. O'Conner, D. J. Schwab, and D. E. Dietrich, Numerical simulation of internal Kelvin waves and coastal upwelling fronts, *J. Phys. Oceanogr.*, *27*, 1197-1215, 1997.

Bennett, J. R., A theory of large amplitude Kelvin waves, *J. Phys. Oceanogr.*, *3*, 57-60, 1973.

Cannon, G. A., Wind effects on currents observed in Juan de Fuca submarine canyon, *J. Phys. Oceanogr.*, *2*, 281-285, 1972.

Cardone, V. J., A. T. Cox, J. A. Greenwood, D. J. Evans, H. Feldman, S. M. Glenn, and T. R. Keen, Hindcast study of wind, wave and current fields in Hurricane Andrew, Gulf of Mexico, final report to Miner. Manage. Serv., Herndon, Va., 1994.

Carrasco, A. C., Internal tides in Dixon Entrance, Ph.D. thesis, 173 pp., Univ. of B. C., Vancouver, B. C., Canada, 1998.

Chen, C., and L. Xie, A numerical study of wind-induced, near-inertial oscillations over the Texas-Louisiana shelf, *J. Geophys. Res.*, *102*, 15,583-15,593, 1997.

Chen, C., R. O. Reid, and W. D. Nowlin Jr., Near-inertial oscillations over the Texas-Louisiana shelf, *J. Geophys. Res.*, *101*, 3509-3524, 1996.

Chen, X., and S. E. Allen, The influence of canyons on shelf currents: A theoretical study, *J. Geophys. Res.*, *101*, 18,043-18,059, 1996.

Cooper, C., and J. D. Thompson, Hurricane-generated currents on the outer continental shelf, 1, Model formulation and verification, *J. Geophys. Res.*, *94*, 12,513-12,539, 1989.

Csanady, G. T., *Circulation in the Coastal Ocean*, 279 pp., D. Reidel, Norwell, Mass., 1984.

Durrieu de Madron, X., Hydrography and nepheloid structure in the Grand-Rhône canyon, *Cont. Shelf Res.*, *14*, 457-477, 1994.

Fandry, C. B., and R. K. Steedman, Modelling the dynamics of the transient, barotropic response of continental shelf waters to tropical cyclones, *Cont. Shelf Res.*, *14*, 1723-1750, 1994.

Fandry, C. B., L. M. Leslie, and R. K. Steedman, Kelvin-type coastal surges generated by tropical cyclones, *J. Phys. Oceanogr.*, *14*, 582-593, 1984.

Gill, A. E., *Atmosphere-Ocean Dynamics*, 662 pp., Academic Press, San Diego, Calif., 1982.

Grimshaw, R., Large-scale, low-frequency response on the continental shelf due to localized atmospheric forcing systems, *J. Phys. Oceanogr.*, *18*, 1906-1919, 1988.

Hazelworth, J. B., Water temperature variations resulting from hurricanes, *J. Geophys. Res.*, *73*, 5105-5123, 1968.

Hearn, C. J., and P. E. Holloway, A three-dimensional barotropic model of the response of the Australian north west shelf to tropical cyclones, *J. Phys. Oceanogr.*, *20*, 60-80, 1990.

Hickey, B. M., The response of a steep-sided, narrow canyon to time-variable wind forcing, *J. Phys. Oceanogr.*, *27*, 697-726, 1997.

Holloway, P. E., A numerical model of internal tides with application to the Australian north west shelf, *J. Phys. Oceanogr.*, *26*, 21-37, 1996.

Hotchkiss, F. S., and C. Wunsch, Internal waves in Hudson Canyon with possible geological implications, *Deep Sea Res.*, *29*, 415-442, 1982.

Huthnance, J. M., On coastal trapped waves: Analysis and numerical calculation by inverse iteration, *J. Phys. Oceanogr.*, *8*, 74-92, 1978.

Keen, T. R., and S. M. Glenn, A quantitative skill assessment of numerical hydrodynamic models of coastal currents, in *Estuarine and Coastal Modeling*, vol. IV, edited by M. L. Spaulding and R. T. Cheng, pp. 26-40, Am. Soc. of Civ. Eng., Reston, Va., 1996.

Keen, T. R., and S. M. Glenn, Factors influencing model skill for hindcasting shallow water currents during Hurricane Andrew, *J. Atmos. Oceanic Technol.*, *15*, 221-236, 1998.

Keen, T. R., and S. M. Glenn, Shallow water currents during Hurricane Andrew, *J. Geophys. Res.*, *104*, 23,443-23,458, 1999.

Klinck, J. M., Circulation near submarine canyons: A modeling study, *J. Geophys. Res.*, *101*, 1211-1223, 1996.

Kundu, P. K., An analysis of inertial oscillations observed near the Oregon coast, *J. Phys. Oceanogr.*, *6*, 879-893, 1976.

Kundu, P. K., A two-dimensional model of inertial oscillations generated by a propagating wind field, *J. Phys. Oceanogr.*, *16*, 1399-1411, 1986.

Mellor, G. L., Users guide for a three-dimensional, primitive equation, numerical ocean model, report, 35 pp., Atmos. and Ocean Sci. Program, Princeton Univ., Princeton, N. J., 1993.

Mellor, G. L., and T. Yamada, Development of a turbulence closure model for geophysical fluid problems, *Rev. Geophys.*, *20*, 851-875, 1982.

Millot, C., and M. Crepon, Inertial oscillations on the continental shelf of the Gulf of Lions–Observations and theory, *J. Phys. Oceanogr.*, *11*, 639-657, 1981.

Niwa, Y., and T. Hibiya, Nonlinear processes of energy transfer from traveling hurricanes to the deep ocean internal wave field, *J. Geophys. Res.*, *102*, 12,469-12,477, 1997.

Oey, L., and P. Chen, A nested-grid ocean model: With application to the simulation of meanders and eddies in the Norwegian coastal current, *J. Geophys. Res.*, *97*, 20,063-20,086, 1992.

Perénne, N., J. Verron, and D. Renouard, Rectified barotropic flow over a submarine canyon, *J. Phys. Oceanogr.*, *27*, 1868-1893, 1997.

Petruncio, E. T., Observations and modeling of the internal tide in a submarine canyon, Ph.D. thesis, 176 pp., Nav. Postgrad. Sch., Monterey, Calif., 1996.

Petruncio, E. T., Observations of the internal tide in Monterey Canyon, *J. Phys. Oceanogr.*, *28*, 1873-1903, 1998.

Press, W. H., S. A. Teukolsky, W. T. Vetterling, and B. P. Flannery, *Numerical Recipes*, 963 pp., Cambridge Univ. Press, New York, 1992.

Schott, F., Spatial structure of inertial-period motions in a two-layered sea, based on observations, *J. Mar. Res.*, *29*, 85-102, 1971.

Smith, N. P., Response of Florida Atlantic shelf waters to Hurricane David, *J. Geophys. Res.*, *87*, 2007-2016, 1982.

Smith, P. C., Inertial oscillations near the coast of Nova Scotia during CASP, *Atmos. Ocean*, *27*, 181-209, 1989.

Tang, M. T., and R. Grimshaw, A modal analysis of coastally trapped waves generated by tropical cyclones, *J. Phys. Oceanogr.*, *25*, 1577-1598, 1995.

Tang, M. T., P. Holloway, and R. Grimshaw, A numerical study of the storm surge generated by Tropical Cyclone Jane, *J. Phys. Oceanogr.*, *27*, 963-976, 1997.

Thompson, E. F., and V. J. Cardone, Practical modelling of hurricane surface wind fields, *J. Water., Port Coastal Ocean Eng.*, *122* (4), 195-205, 1994.

S. E. Allen, Department of Earth and Ocean Sciences, University of British Columbia, Vancouver, BC, Canada V6T 1Z4. (allen@ocgy.ubc.ca)

T. R. Keen, Oceanography Division, Naval Research Laboratory, Code 7322, Stennis Space Center, MS 39529. (keen@nrlssc.navy.mil)

(Received May 21, 1999; revised May 24, 2000;
accepted July 26, 2000.)